THE EUROPEAN PHYSICAL JOURNAL C

Subjet distributions in deep inelastic scattering at HERA

The ZEUS Collaboration

S. Chekanov[1], M. Derrick[1], S. Magill[1], B. Musgrave[1], D. Nicholass[1,c], J. Repond[1], R. Yoshida[1], M.C.K. Mattingly[2], P. Antonioli[3], G. Bari[3], L. Bellagamba[3], D. Boscherini[3], A. Bruni[3], G. Bruni[3], F. Cindolo[3], M. Corradi[3], G. Iacobucci[3], A. Margotti[3], R. Nania[3], A. Polini[3], S. Antonelli[4], M. Basile[4], M. Bindi[4], L. Cifarelli[4], A. Contin[4], S. De Pasquale[4,d], G. Sartorelli[4], A. Zichichi[4], D. Bartsch[5], I. Brock[5], H. Hartmann[5], E. Hilger[5], H.-P. Jakob[5], M. Jüngst[5], A.E. Nuncio-Quiroz[5], E. Paul[5], U. Samson[5], V. Schönberg[5], R. Shehzadi[5], M. Wlasenko[5], N.H. Brook[6], G.P. Heath[6], J.D. Morris[6], M. Kaur[7], P. Kaur[7,e], I. Singh[7,e], M. Capua[8], S. Fazio[8], A. Mastroberardino[8], M. Schioppa[8], G. Susinno[8], E. Tassi[8], J.Y. Kim[9], Z.A. Ibrahim[10], F. Mohamad Idris[10], B. Kamaluddin[10], W.A.T. Wan Abdullah[10], Y. Ning[11], Z. Ren[11], F. Sciulli[11], J. Chwastowski[12], A. Eskreys[12], J. Figiel[12], A. Galas[12], K. Olkiewicz[12], B. Pawlik[12], P. Stopa[12], L. Zawiejski[12], L. Adamczyk[13], T. Bołd[13], I. Grabowska-Bołd[13], D. Kisielewska[13], J. Łukasik[13,f], M. Przybycień[13], L. Suszycki[13], A. Kotański[14,g], W. Słomiński[14,h], O. Behnke[15], U. Behrens[15], C. Blohm[15], A. Bonato[15], K. Borras[15], D. Bot[15], R. Ciesielski[15], N. Coppola[15], S. Fang[15], J. Fourletova[15,i], A. Geiser[15], P. Göttlicher[15,j], J. Grebenyuk[15], I. Gregor[15], T. Haas[15,a], W. Hain[15], A. Hüttmann[15], F. Januschek[15], B. Kahle[15], I.I. Katkov[15,k], U. Klein[15,l], U. Kötz[15], H. Kowalski[15], M. Lisovyi[15], E. Lobodzinska[15], B. Löhr[15], R. Mankel[15,m], I.-A. Melzer-Pellmann[15], S. Miglioranzi[15,n], A. Montanari[15], T. Namsoo[15], D. Notz[15,m], A. Parenti[15], L. Rinaldi[15,o], P. Roloff[15], I. Rubinsky[15], U. Schneekloth[15], A. Spiridonov[15,p], D. Szuba[15,q], J. Szuba[15,r], T. Theedt[15], J. Ukleja[15,s], G. Wolf[15], K. Wrona[15], A.G. Yagües Molina[15], C. Youngman[15], W. Zeuner[15,m], V. Drugakov[16], W. Lohmann[16], S. Schlenstedt[16], G. Barbagli[17], E. Gallo[17], P.G. Pelfer[18], A. Bamberger[19], D. Dobur[19], F. Karstens[19], N.N. Vlasov[19,t], P.J. Bussey[20,u], A.T. Doyle[20], W. Dunne[20], M. Forrest[20], M. Rosin[20], D.H. Saxon[20], I.O. Skillicorn[20], I. Gialas[21,v], K. Papageorgiu[21], U. Holm[22], R. Klanner[22], E. Lohrmann[22], H. Perrey[22], P. Schleper[22], T. Schörner-Sadenius[22], J. Sztuk[22], H. Stadie[22], M. Turcato[22], C. Foudas[23], C. Fry[23], K.R. Long[23], A.D. Tapper[23], T. Matsumoto[24], K. Nagano[24], K. Tokushuku[24,w], S. Yamada[24], Y. Yamazaki[24,x], A.N. Barakbaev[25], E.G. Boos[25], N.S. Pokrovskiy[25], B.O. Zhautykov[25], V. Aushev[26,y], O. Bachynska[26], M. Borodin[26], I. Kadenko[26], A. Kozulia[26], V. Libov[26], D. Lontkovskyi[26], I. Makarenko[26], I. Sorokin[26], A. Verbytskyi[26], O. Volynets[26], D. Son[27], J. de Favereau[28], K. Piotrzkowski[28], F. Barreiro[29], C. Glasman[29], M. Jimenez[29], L. Labarga[29], J. del Peso[29], E. Ron[29], M. Soares[29], J. Terrón[29], C. Uribe-Estrada[29], M. Zambrana[29], F. Corriveau[30], C. Liu[30], J. Schwartz[30], R. Walsh[30], C. Zhou[30], T. Tsurugai[31], A. Antonov[32], B.A. Dolgoshein[32], D. Gladkov[32], V. Sosnovtsev[32], A. Stifutkin[32], S. Suchkov[32], R.K. Dementiev[33], P.F. Ermolov[33,b], L.K. Gladilin[33], Y.A. Golubkov[33], L.A. Khein[33], I.A. Korzhavina[33], V.A. Kuzmin[33], B.B. Levchenko[33,z], O.Y. Lukina[33], A.S. Proskuryakov[33], L.M. Shcheglova[33], D.S. Zotkin[33], I. Abt[34], A. Caldwell[34], D. Kollar[34], B. Reisert[34], W.B. Schmidke[34], G. Grigorescu[35], A. Keramidas[35], E. Koffeman[35], P. Kooijman[35], A. Pellegrino[35], H. Tiecke[35], M. Vázquez[35,n], L. Wiggers[35], N. Brümmer[36], B. Bylsma[36], L.S. Durkin[36], A. Lee[36], T.Y. Ling[36], P.D. Allfrey[37], M.A. Bell[37], A.M. Cooper-Sarkar[37], R.C.E. Devenish[37], J. Ferrando[37], B. Foster[37], C. Gwenlan[37,aa], K. Horton[37,ab], K. Oliver[37], A. Robertson[37], R. Walczak[37], A. Bertolin[38], F. Dal Corso[38], S. Dusini[38], A. Longhin[38], L. Stanco[38], P. Bellan[39], R. Brugnera[39], R. Carlin[39], A. Garfagnini[39], S. Limentani[39], B.Y. Oh[40], A. Raval[40], J.J. Whitmore[40,ac], Y. Iga[41], G. D'Agostini[42], G. Marini[42], A. Nigro[42], J.E. Cole[43,ad], J.C. Hart[43], H. Abramowicz[44,ae], R. Ingbir[44], S. Kananov[44], A. Levy[44], A. Stern[44], M. Kuze[45], J. Maeda[45], R. Hori[46], S. Kagawa[46,af], N. Okazaki[46], S. Shimizu[46], T. Tawara[46], R. Hamatsu[47], H. Kaji[47,ag], S. Kitamura[47,ah], O. Ota[47,ai], Y.D. Ri[47], M. Costa[48], M.I. Ferrero[48], V. Monaco[48], R. Sacchi[48], V. Sola[48], A. Solano[48], M. Arneodo[49], M. Ruspa[49], S. Fourletov[50,i], J.F. Martin[50], T.P. Stewart[50], S.K. Boutle[51,v], J.M. Butterworth[51], T.W. Jones[51], J.H. Loizides[51], M. Wing[51,aj], B. Brzozowska[52], J. Ciborowski[52,ak], G. Grzelak[52], P. Kulinski[52], P. Łużniak[52,al], J. Malka[52,al], R.J. Nowak[52], J.M. Pawlak[52], W. Perlanski[52,al], T. Tymieniecka[52,am], A.F. Żarnecki[52], M. Adamus[53], P. Plucinski[53,an], A. Ukleja[53], Y. Eisenberg[54], D. Hochman[54], U. Karshon[54], E. Brownson[55], D.D. Reeder[55], A.A. Savin[55], W.H. Smith[55], H. Wolfe[55], S. Bhadra[56], C.D. Catterall[56], Y. Cui[56], G. Hartner[56], S. Menary[56], U. Noor[56], J. Standage[56], J. Whyte[56]

[1] Argonne National Laboratory, Argonne, IL 60439-4815, USA[bb]

[2] Andrews University, Berrien Springs, MI 49104-0380, USA

[3] INFN Bologna, Bologna, Italy[as]

[4] University and INFN Bologna, Bologna, Italy[as]

[5] Physikalisches Institut der Universität Bonn, Bonn, Germany[ap]

[6] H.H. Wills Physics Laboratory, University of Bristol, Bristol, UK[ba]

[7] Department of Physics, Panjab University, Chandigarh, India

[8] Physics Department and INFN, Calabria University, Cosenza, Italy[as]

[9] Chonnam National University, Kwangju, South Korea

[10] Jabatan Fizik, Universiti Malaya, 50603 Kuala Lumpur, Malaysia[bf]

[11] Nevis Laboratories, Columbia University, Irvington on Hudson, NY 10027, USA[bc]

[12] The Henryk Niewodniczanski Institute of Nuclear Physics, Polish Academy of Sciences, Cracow, Poland[aw]

[13] Faculty of Physics and Applied Computer Science, AGH-University of Science and Technology, Cracow, Poland[bd]

[14] Department of Physics, Jagellonian University, Cracow, Poland

[15] Deutsches Elektronen-Synchrotron DESY, Hamburg, Germany

[16] Deutsches Elektronen-Synchrotron DESY, Zeuthen, Germany

[17] INFN Florence, Florence, Italy[as]

[18] University and INFN Florence, Florence, Italy[as]

[19] Fakultät für Physik der Universität Freiburg i.Br., Freiburg i.Br., Germany[ap]

[20] Department of Physics and Astronomy, University of Glasgow, Glasgow, UK[ba]

[21] Department of Engineering in Management and Finance, Univ. of Aegean, Mytilene, Greece

[22] Institute of Exp. Physics, Hamburg University, Hamburg, Germany[ap]

[23] High Energy Nuclear Physics Group, Imperial College London, London, UK[ba]

[24] Institute of Particle and Nuclear Studies, KEK, Tsukuba, Japan[at]

[25] Institute of Physics and Technology of Ministry of Education and Science of Kazakhstan, Almaty, Kazakhstan

[26] Institute for Nuclear Research, National Academy of Sciences, Kiev and Kiev National University, Kiev, Ukraine

[27] Center for High Energy Physics, Kyungpook National University, Daegu, South Korea[au]

[28] Institut de Physique Nucléaire, Université Catholique de Louvain, Louvain-la-Neuve, Belgium[be]

[29] Departamento de Física Teórica, Universidad Autónoma de Madrid, Madrid, Spain[az]

[30] Department of Physics, McGill University, Montréal, Québec, Canada H3A 2T8[ao]

[31] Faculty of General Education, Meiji Gakuin University, Yokohama, Japan[at]

[32] Moscow Engineering Physics Institute, Moscow, Russia[ax]

[33] Institute of Nuclear Physics, Moscow State University, Moscow, Russia[ay]

[34] Max-Planck-Institut für Physik, Munich, Germany

[35] NIKHEF and University of Amsterdam, Amsterdam, Netherlands[av]

[36] Physics Department, Ohio State University, Columbus, OH 43210, USA[bb]

[37] Department of Physics, University of Oxford, Oxford, UK[ba]

[38] INFN Padova, Padova, Italy[as]

[39] Dipartimento di Fisica dell' Università and INFN, Padova, Italy[as]

[40] Department of Physics, Pennsylvania State University, University Park, PA 16802, USA[bc]

[41] Polytechnic University, Sagamihara, Japan[at]

[42] Dipartimento di Fisica, Università 'La Sapienza' and INFN, Rome, Italy[as]

[43] Rutherford Appleton Laboratory, Chilton, Didcot, Oxon, UK[ba]

[44] Raymond and Beverly Sackler Faculty of Exact Sciences, School of Physics, Tel Aviv University, Tel Aviv, Israel[ar]

[45] Department of Physics, Tokyo Institute of Technology, Tokyo, Japan[at]

[46] Department of Physics, University of Tokyo, Tokyo, Japan[at]

[47] Department of Physics, Tokyo Metropolitan University, Tokyo, Japan[at]

[48] Università di Torino and INFN, Torino, Italy[as]

[49] Università del Piemonte Orientale, Novara, and INFN, Torino, Italy[as]

[50] Department of Physics, University of Toronto, Toronto, Ontario, Canada M5S 1A7[ao]

[51] Physics and Astronomy Department, University College London, London, UK[ba]

[52] Institute of Experimental Physics, Warsaw University, Warsaw, Poland

[53] Institute for Nuclear Studies, Warsaw, Poland

[54] Department of Particle Physics, Weizmann Institute, Rehovot, Israel[aq]

[55] Department of Physics, University of Wisconsin, Madison, WI 53706, USA[bb]

[56] Department of Physics, York University, Toronto, Ontario, Canada M3J 1P3[ao]

[a] e-mail: tobias.haas@desy.de

[b] Deceased.

[c] Also affiliated with University College London, United Kingdom.

[d] Now at University of Salerno, Italy.

Eur. Phys. J. C (2009) 63: 527–548

529

Abstract Subjet distributions were measured in neutral current deep inelastic *ep* scattering with the ZEUS detector at HERA using an integrated luminosity of 81.7 pb^{-1}. Jets were identified using the k_T cluster algorithm in the laboratory frame. Subjets were defined as jet-like substructures identified by a reapplication of the cluster algorithm at a smaller value of the resolution parameter y_{cut}. Measurements of subjet distributions for jets with exactly two subjets for $y_{cut} = 0.05$ are presented as functions of observables sensitive to the pattern of parton radiation and to the colour

coherence between the initial and final states. Perturbative QCD predictions give an adequate description of the data.

1 Introduction

Jet production in *ep* collisions provides a wide testing ground of perturbative QCD (pQCD). Measurements of differential cross sections for jet production [1–18] have allowed for detailed studies of parton dynamics, tests of the proton and photon parton distribution functions (PDFs) as

530

Eur. Phys. J. C (2009) 63: 527–548

well as precise determinations of the strong coupling constant, α_s.

Gluon emission from primary quarks was investigated [19, 20] by means of the internal structure of jets; these type of studies gave insight into the transition between a parton produced in a hard process and the experimentally observable jet of hadrons. The pattern of parton radiation within a jet is dictated in QCD by the splitting functions. These functions, $P_{ab}(z, \mu)$ with $a, b = q$ or g, are interpreted as the probability that a parton of type b, having radiated a parton of type a, is left with a fraction z of the longitudinal momentum of the parent parton and a transverse momentum squared smaller than μ^2, where μ is the typical hard scale of the process. The splitting functions are calculable as power series in α_s. Thus, the characteristics of jet substructure provide direct access to the QCD splitting functions and their dependence on the scale.

The understanding of jet substructure is also important in the context of jet identification in boosted systems, like hadronic top decays [21, 22] or $b\bar{b}$ final states at LHC [23]. The first example calls for a direct application of jet substructure, the second requires knowledge about jet substructure to distinguish between single- and double-quark induced jets. This paper presents a study of jet substructure in a more controlled hadronic-type environment than that provided by hadron–hadron colliders.

Jet production in neutral current (NC) deep inelastic scattering (DIS) was previously used to study the mean subjet multiplicity [19] and the mean integrated jet shape [20] with values of $\alpha_s(M_Z)$ extracted from those measurements. In the present study, the pattern of QCD radiation is investigated by means of the subjet topology, providing a more stringent test of the pQCD calculations.

In this paper, measurements of normalized differential subjet cross sections for those jets which contain two subjets at a given resolution scale are presented. The measurements were done as functions of the ratio between the subjet transverse energy and that of the jet, $E_T^{\text{sbj}}/E_T^{\text{jet}}$, the difference between the subjet pseudorapidity[1] (azimuth) and that of the jet, $\eta^{\text{sbj}} - \eta^{\text{jet}}$ ($|\phi^{\text{sbj}} - \phi^{\text{jet}}|$), and α^{sbj}, the angle, as viewed from the jet center, between the subjet with higher transverse energy and the proton beam line in the pseudorapidity–azimuth plane (see Fig. 1). The predictions of pQCD at next-to-leading order (NLO) were compared to the data.

Fig. 1 Schematic representation of the α^{sbj} variable

2 Jets and subjets

Inclusive deep inelastic lepton–proton scattering can be described in terms of the kinematic variables x, y and Q^2. The variable Q^2 is defined as $Q^2 = -q^2 = -(k - k')^2$, where k and k' are the four-momenta of the incoming and scattered lepton, respectively. Bjorken x is defined as $x = Q^2/(2P \cdot q)$, where P is the four-momentum of the incoming proton. The fraction of the lepton energy transferred to the proton in its rest frame is given by $y = P \cdot q/P \cdot k$. The variables x, y and Q^2 are related by $Q^2 = sxy$, where s is the squared center-of-mass energy.

The analysis of subjets presented in this paper was performed using the laboratory frame. In this frame, the calculations of the subjet distributions can be performed up to $\mathcal{O}(\alpha_s^2)$, i.e. NLO, with jets consisting of up to three partons. The analysis used events with high virtuality of the exchanged boson, Q^2; at low values of Q^2, the sample of events with at least one jet of high E_T^{jet} ($E_T^{\text{jet}} \gg \sqrt{Q^2}$) is dominated by dijet events. In that case, the calculations include jets consisting of up to only two partons and, therefore, correspond to lowest-order predictions of jet substructure.

The k_T cluster algorithm [24] was used in the longitudinally invariant inclusive mode [25] to define jets in the hadronic final state. Subjets [26–29] were resolved within a jet by considering all particles associated with the jet and repeating the application of the k_T cluster algorithm until, for every pair of particles i and j the quantity $d_{ij} = \min(E_{T,i}, E_{T,j})^2 \cdot ((\eta_i - \eta_j)^2 + (\phi_i - \phi_j)^2)$, where $E_{T,i}$, η_i and ϕ_i are the transverse energy, pseudorapidity and azimuth of particle i, respectively, was greater than $d_{\text{cut}} = y_{\text{cut}} \cdot (E_T^{\text{jet}})^2$. All remaining clusters were called subjets.

---

[1] The ZEUS coordinate system is a right-handed Cartesian system, with the Z axis pointing in the proton beam direction, referred to as the "forward direction", and the X axis pointing left towards the center of HERA. The coordinate origin is at the nominal interaction point. The pseudorapidity is defined as $\eta = -\ln(\tan\frac{\theta}{2})$, where the polar angle θ is taken with respect to the proton beam direction.
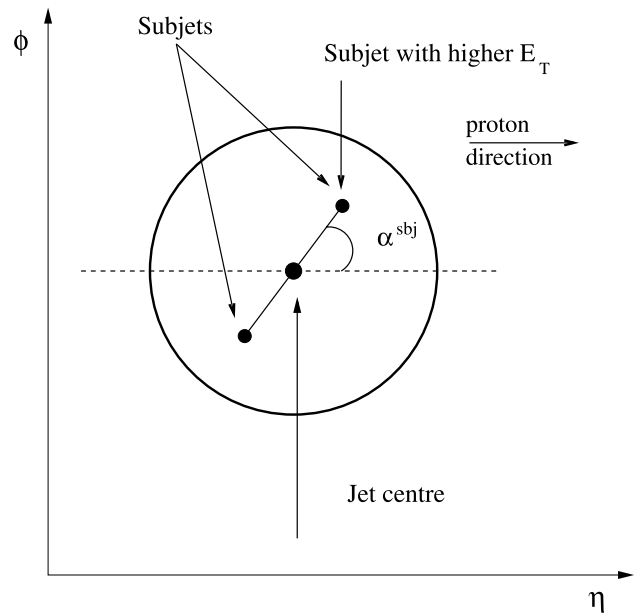
The subjet multiplicity depends upon the value chosen for the resolution parameter y_{cut}. Subjet distributions were studied for those jets with exactly two subjets at a value of the resolution parameter of $y_{\text{cut}} = 0.05$. This value of y_{cut} was chosen as a compromise between resolution, size of the hadronization correction factors and statistics. The effect of the parton-to-hadron corrections on the shape of the subjet distributions becomes increasingly larger as y_{cut} decreases. On the other hand, the number of jets with exactly two subjets decreases rapidly as y_{cut} increases.

Subjet distributions were studied as functions of $E_T^{\text{sbj}}/E_T^{\text{jet}}$, $\eta^{\text{sbj}} - \eta^{\text{jet}}$, $|\phi^{\text{sbj}} - \phi^{\text{jet}}|$ and α^{sbj}. One of the goals of this study was to investigate the extent to which pQCD calculations are able to reproduce the observed distributions. In addition, the dependence of the splitting functions $P_{ab}(z, \mu)$ on z can be investigated using the $E_T^{\text{sbj}}/E_T^{\text{jet}}$ distribution. The splitting functions at leading order (LO) do not depend on μ but acquire a weak dependence due to higher-order corrections. Such a dependence can be investigated by measuring the subjet distributions in different regions of E_T^{jet} or Q^2.

The substructure of jets consisting of a quark-gluon pair (the quark-induced process $eq \rightarrow eqg$) or a quark-antiquark pair (the gluon-induced process $eg \rightarrow eq\bar{q}$) are predicted to be different (see Sect. 8.1). Furthermore, the relative contributions of quark- and gluon-induced processes vary with Bjorken x and Q^2. The predicted difference mentioned above is amenable to experimental investigation by comparing the shape of the subjet distributions in different regions of x and Q^2.

Color coherence leads to a suppression of soft-gluon radiation in certain regions of phase space. The effects of color coherence between the initial and final states have been studied in hadron–hadron collisions [30]. These effects are also expected to appear in lepton–hadron collisions. For the process $eq \rightarrow eqg$, color coherence implies a tendency of the subjet with lower (higher) transverse energy, $E_{T,\text{low}}^{\text{sbj}}$ ($E_{T,\text{high}}^{\text{sbj}}$), to have $\eta^{\text{sbj}} - \eta^{\text{jet}} > 0$ ($\eta^{\text{sbj}} - \eta^{\text{jet}} < 0$). The variable α^{sbj}, defined in close analogy to the variables used to study color coherence in hadron–hadron collisions [30], reflects directly whether the subjet with the lower transverse energy has a tendency to be emitted towards the proton beam direction.

3 Experimental set-up

A detailed description of the ZEUS detector can be found elsewhere [31, 32]. A brief outline of the components most relevant for this analysis is given below.

Charged particles were tracked in the central tracking detector (CTD) [33–35], which operated in a magnetic field of 1.43 T provided by a thin superconducting solenoid. The CTD consisted of 72 cylindrical drift-chamber layers, organized in nine superlayers covering the polar-angle region $15° < \theta < 164°$. The transverse-momentum resolution for full-length tracks can be parameterized as $\sigma(p_T)/p_T = 0.0058 p_T \oplus 0.0065 \oplus 0.0014/p_T$, with p_T in GeV. The tracking system was used to measure the interaction vertex with a typical resolution along (transverse to) the beam direction of 0.4 (0.1) cm and to cross-check the energy scale of the calorimeter.

The high-resolution uranium–scintillator calorimeter (CAL) [36–39] covered 99.7% of the total solid angle and consisted of three parts: the forward (FCAL), the barrel (BCAL) and the rear (RCAL) calorimeters. Each part was subdivided transversely into towers and longitudinally into one electromagnetic section and either one (in RCAL) or two (in BCAL and FCAL) hadronic sections. The smallest subdivision of the calorimeter was called a cell. Under test-beam conditions, the CAL single-particle relative energy resolutions were $\sigma(E)/E = 0.18/\sqrt{E}$ for electrons and $\sigma(E)/E = 0.35/\sqrt{E}$ for hadrons, with E in GeV.

The luminosity was measured from the rate of the bremsstrahlung process $ep \rightarrow e\gamma p$. The resulting small-angle energetic photons were measured by the luminosity monitor [40–42], a lead–scintillator calorimeter placed in the HERA tunnel at $Z = -107$ m.

4 Data selection

The data were collected during the running period 1998–2000, when HERA operated with protons of energy $E_p = 920$ GeV and electrons or positrons[2] of energy $E_e = 27.5$ GeV, and correspond to an integrated luminosity of 81.7 ± 1.9 pb^{-1}.

Neutral current DIS events were selected offline using criteria similar to those reported previously [20]. The main steps are given below.

A reconstructed event vertex consistent with the nominal interaction position was required and cuts based on tracking information were applied to reduce the contamination from beam-induced and cosmic-ray background. The scattered-electron candidate was identified using the pattern of energy deposits in the CAL [43, 44]. The energy, E_e', and polar angle, θ_e, of the electron candidate were also determined from the CAL measurements. The double-angle method [45, 46], which uses θ_e and an angle γ that corresponds, in the quark-parton model, to the direction of the scattered quark, was used to reconstruct Q^2. The angle γ was reconstructed using the CAL measurements of the hadronic final state.

532

Eur. Phys. J. C (2009) 63: 527–548

Electron candidates were required to have an energy $E'_e > 10$ GeV, to ensure a high and well understood electron-finding efficiency and to suppress background from photoproduction. The inelasticity variable, y, as reconstructed using the electron energy and polar angle, was required to be below 0.95; this condition removed events in which fake electron candidates from photoproduction background were found in the FCAL. The requirement $38 < (E - p_Z) < 65$ GeV, where E is the total CAL energy and p_Z is the Z component of the energy measured in the CAL cells, was applied to remove events with large initial-state radiation and to reduce further the photoproduction background. Remaining cosmic rays and beam-related background were rejected by requiring the total missing transverse momentum, p_T^{miss}, to be small compared to the total transverse energy, E_T^{tot}, $p_T^{\text{miss}}/\sqrt{E_T^{\text{tot}}} < 3 \sqrt{\text{GeV}}$. The kinematic range was restricted to $Q^2 > 125$ GeV^2.

The k_T cluster algorithm was used in the longitudinally invariant inclusive mode to reconstruct jets in the measured hadronic final state from the energy deposits in the CAL cells. The jet algorithm was applied after excluding those cells associated with the scattered-electron candidate. Jet transverse-energy corrections were computed using the method developed in a previous analysis [20]. Events were required to have at least one jet of $E_T^{\text{jet}} > 14$ GeV and $-1 < \eta^{\text{jet}} < 2.5$. The final sample of 128986 events contained 132818 jets, of which 21162 jets had exactly two subjets at $y_{\text{cut}} = 0.05$.

5 Monte Carlo simulation

Samples of events were generated to determine the response of the detector to jets of hadrons and the correction factors necessary to obtain the hadron-level subjet cross sections. The hadron level is defined as those hadrons with lifetime $\tau \geq 10$ ps. The generated events were passed through the GEANT 3.13-based [47] ZEUS detector- and trigger-simulation programs [32]. They were reconstructed and analysed applying the same program chain as to the data.

Neutral current DIS events including radiative effects were simulated using the HERACLES 4.6.1 [48, 49] program with the DJANGOH 1.1 [50, 51] interface to the hadronization programs. HERACLES includes corrections for initial- and final-state radiation, vertex and propagator terms, and two-boson exchange. The QCD cascade is simulated using the color-dipole model (CDM) [52–55] including the LO QCD diagrams as implemented in ARIADNE 4.08 [56, 57] and, alternatively, with the MEPS model of LEPTO 6.5 [58]. The CTEQ5D [59] proton PDFs were used for these simulations. Fragmentation into hadrons is performed using the Lund string model [60] as implemented in JETSET [61–64].

The jet search was performed on the Monte Carlo (MC) events using the energy measured in the CAL cells in the same way as for the data. The same jet algorithm was also applied to the final-state particles (hadron level) and to the partons available after the parton shower (parton level) to compute hadronization correction factors (see Section 6).

6 QCD calculations

The $\mathcal{O}(\alpha_s^2)$ NLO QCD calculations used to compare with the data are based on the program DISENT [65]. The calculations used a generalized version of the subtraction method [66] and were performed in the massless $\overline{\text{MS}}$ renormalization and factorization schemes. The number of flavors was set to five; the renormalization (μ_R) and factorization (μ_F) scales were set to $\mu_R = \mu_F = Q$; α_s was calculated at two loops using $\Lambda_{\overline{\text{MS}}}^{(5)} = 220$ MeV which corresponds to $\alpha_s(M_Z) = 0.118$. The ZEUS-S [67] parameterizations of the proton PDFs were used. The results obtained with DISENT were cross-checked by using the program NLOJET++ [68].

Since the measurements refer to jets of hadrons, whereas the QCD calculations refer to jets of partons, the predictions were corrected to the hadron level using the MC samples described in Sect. 5. The multiplicative correction factor, C_{had}, defined as the ratio of the cross section for subjets of hadrons to that of partons, was estimated with the LEPTO-MEPS model, since it reproduced the shape of the QCD calculations better[3]. The normalized cross-section calculations changed typically by less than $\pm 20\%$ upon application of the parton-to-hadron corrections, except at the edges of the distributions, where they changed by up to $\pm 50\%$. Other effects not accounted for in the calculations, namely QED radiative corrections and Z^0 exchange, were found to be very small for the normalized cross-section calculations and neglected.

The dominant source of theoretical uncertainty is in the modeling of the parton shower, which was estimated by using different models (see Sect. 5) to calculate the parton-to-hadron correction factors. As examples of the size of the uncertainty, average values of the effect on the normalized cross section as functions of $E_T^{\text{sbj}}/E_T^{\text{jet}}$, $\eta^{\text{sbj}} - \eta^{\text{jet}}$, $|\phi^{\text{sbj}} - \phi^{\text{jet}}|$ and α^{sbj} are 5.6%, 13.2%, 7.6% and 5.3%, respectively. Other uncertainties, such as those arising from higher-order terms, choice of μ_F, those on the proton PDFs and that on $\alpha_s(M_Z)$, were investigated and found to be small in comparison. These uncertainties were added in

---

[3]The HERWIG model [69–71] has not been used since its predictions exhibited a different dependence than the calculations [19].

Eur. Phys. J. C (2009) 63: 527–548

533

quadrature and are shown as hatched bands in the figures.

7 Corrections and systematic uncertainties

The sample of events generated with CDM, after applying the same offline selection as for the data, gives a reasonably good description of the measured distributions of the kinematic, jet and subjet variables; the description provided by the MEPS sample is somewhat poorer. The comparison of the measured subjet distributions and the MC simulations is shown in Fig. 2.

The normalized differential cross sections were obtained from the data using the bin-by-bin correction method,

$$\frac{1}{\sigma}\frac{d\sigma_i}{dA} = \frac{1}{\sigma}\frac{N_{\mathrm{data},i}}{\mathcal{L}\cdot\Delta A_i}\cdot\frac{N_{\mathrm{MC},i}^{\mathrm{had}}}{N_{\mathrm{MC},i}^{\mathrm{det}}},$$

where $N_{\mathrm{data},i}$ is the number of subjets in data in bin i of the subjet variable A, $N_{\mathrm{MC},i}^{\mathrm{had}}$ ($N_{\mathrm{MC},i}^{\mathrm{det}}$) is the number of subjets in MC at hadron (detector) level, $\mathcal{L}$ is the integrated luminosity and ΔA_i is the bin width. The MC samples of CDM and MEPS were used to compute the acceptance correction factors to the subjet distributions. These correction factors took into account the efficiency of the trigger, the selection criteria and the purity and efficiency of the jet and subjet reconstruction. The average of the correction factors evaluated with CDM and MEPS were used to obtain the central values of the normalized differential cross sections.

The following sources of systematic uncertainty were considered for the measured subjet cross sections (as examples of the size of the uncertainties, average values of the effect of each uncertainty on the normalized cross section as functions of $E_T^{\mathrm{sbj}}/E_T^{\mathrm{jet}}$, $\eta^{\mathrm{sbj}}-\eta^{\mathrm{jet}}$, $|\phi^{\mathrm{sbj}}-\phi^{\mathrm{jet}}|$ and α^{sbj} are given in parentheses):

- The deviations in the results obtained by using either CDM or MEPS to correct the data from their average were taken to represent systematic uncertainties due to the modeling of the parton shower (0.5%, 2.9%, 2.6%, 1.3%).
- Variations in the simulation of the CAL response to low-energy particles (0.3%, 1.6%, 1.2%, 0.6%).

Other uncertainties, such as those arising from the uncertainty in the absolute energy scale of the jets [1, 2, 73], the uncertainty in the simulation of the trigger and the uncertainty in the absolute energy scale of the electron candidate [74], were investigated and found to be negligible. The systematic uncertainties were added in quadrature to the sta-

Fig. 2 Detector-level normalized subjet data distributions (*dots*) for jets with $E_T^{\mathrm{jet}} > 14$ GeV and $-1 < \eta^{\mathrm{jet}} < 2.5$ which have two subjets for $y_{\mathrm{cut}} = 0.05$ in the kinematic region given by $Q^2 > 125$ GeV^2 as functions of (**a**) $E_T^{\mathrm{sbj}}/E_T^{\mathrm{jet}}$, (**b**) $\eta^{\mathrm{sbj}}-\eta^{\mathrm{jet}}$, (**c**) $|\phi^{\mathrm{sbj}}-\phi^{\mathrm{jet}}|$ and (**d**) α^{sbj}. The statistical uncertainties are smaller than the marker size. For comparison, the distributions of the CDM (*solid histograms*) and MEPS (*dot-dashed histograms*) Monte Carlo models are included
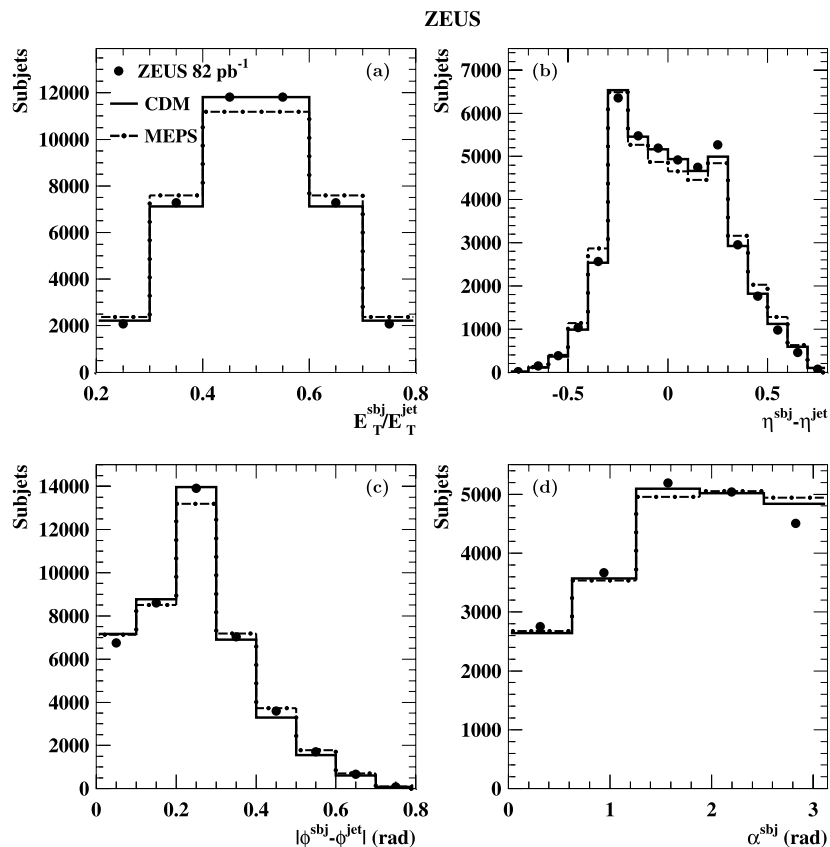
tistical uncertainties and are shown as error bars in the figures.

8 Results

Normalized differential subject cross sections were measured for $Q^2 > 125$ GeV^2 for jets with $E_T^{\rm jet} > 14$ GeV and $-1 < \eta^{\rm jet} < 2.5$ which have exactly two subjets for $y_{\rm cut} = 0.05$.

The distribution of the fraction of transverse energy, $(1/\sigma)(d\sigma/d(E_T^{\rm sbj}/E_T^{\rm jet}))$, is presented in Fig. 3a. It contains two entries per jet and is symmetric with respect to $E_T^{\rm sbj}/E_T^{\rm jet} = 0.5$ by construction. This distribution has a peak for $0.4 < E_T^{\rm sbj}/E_T^{\rm jet} < 0.6$, which shows that the two subjets tend to have similar transverse energies.

The $\eta^{\rm sbj} - \eta^{\rm jet}$ data distribution is shown in Fig. 3b and also has two entries per jet. The measured cross section has a two-peak structure; the dip around $\eta^{\rm sbj} - \eta^{\rm jet} = 0$ is due to the fact that the two subjets are not resolved when they are too close together.

Figure 3c presents the measured normalized cross section as a function of $|\phi^{\rm sbj} - \phi^{\rm jet}|$. There are two entries per jet in this distribution. The distribution has a peak for $0.2 < |\phi^{\rm sbj} - \phi^{\rm jet}| < 0.3$; the suppression around $|\phi^{\rm sbj} - \phi^{\rm jet}| = 0$ also arises from the fact that the two subjets are not resolved when they are too close together.

The data distribution as a function of $\alpha^{\rm sbj}$ (one entry per jet) increases as $\alpha^{\rm sbj}$ increases (see Fig. 3d). This shows that the subjet with higher transverse energy tends to be in the rear direction. This is consistent with the asymmetric peaks observed in the $\eta^{\rm sbj} - \eta^{\rm jet}$ distribution (see Fig. 3b). Figure 4 shows the $\eta^{\rm sbj} - \eta^{\rm jet}$ distribution for those jets which have two subjets with asymmetric $E_T^{\rm sbj}$ ($E_{T,\rm low}^{\rm sbj}/E_T^{\rm jet} < 0.4$, or, equivalently, $E_{T,\rm high}^{\rm sbj}/E_T^{\rm jet} > 0.6$), separately for the subjet with higher and lower $E_T^{\rm sbj}$. It is to be noted that since the jet axis is reconstructed as the transverse-energy-weighted average of the subjet axes, the subjet with higher $E_T^{\rm sbj}$ is constrained to be closer to the jet axis than that of the lower $E_T^{\rm sbj}$ subjet. The measured distributions show that the higher (lower) $E_T^{\rm sbj}$ subjet tends to be in the rear (forward) direction. All these observations support the expectation of the presence of color-coherence effects between the initial and final states and, in particular, the tendency of the subjet with lower $E_T^{\rm sbj}$ to be emitted predominantly towards the proton beam direction.

Fig. 3 Measured normalized differential subjet cross sections (*dots*) for jets with $E_T^{\rm jet} > 14$ GeV and $-1 < \eta^{\rm jet} < 2.5$ which have two subjets for $y_{\rm cut} = 0.05$ in the kinematic region given by $Q^2 > 125$ GeV^2 as functions of **(a)** $E_T^{\rm sbj}/E_T^{\rm jet}$, **(b)** $\eta^{\rm sbj} - \eta^{\rm jet}$, **(c)** $|\phi^{\rm sbj} - \phi^{\rm jet}|$ and **(d)** $\alpha^{\rm sbj}$. The inner error bars represent the statistical uncertainties of the data, the outer error bars show the statistical and systematic uncertainties added in quadrature. In many cases, the error bars are smaller than the marker size and are therefore not visible. For comparison, the NLO QCD predictions (*solid histograms*) are included. The hatched bands represent the theoretical uncertainty
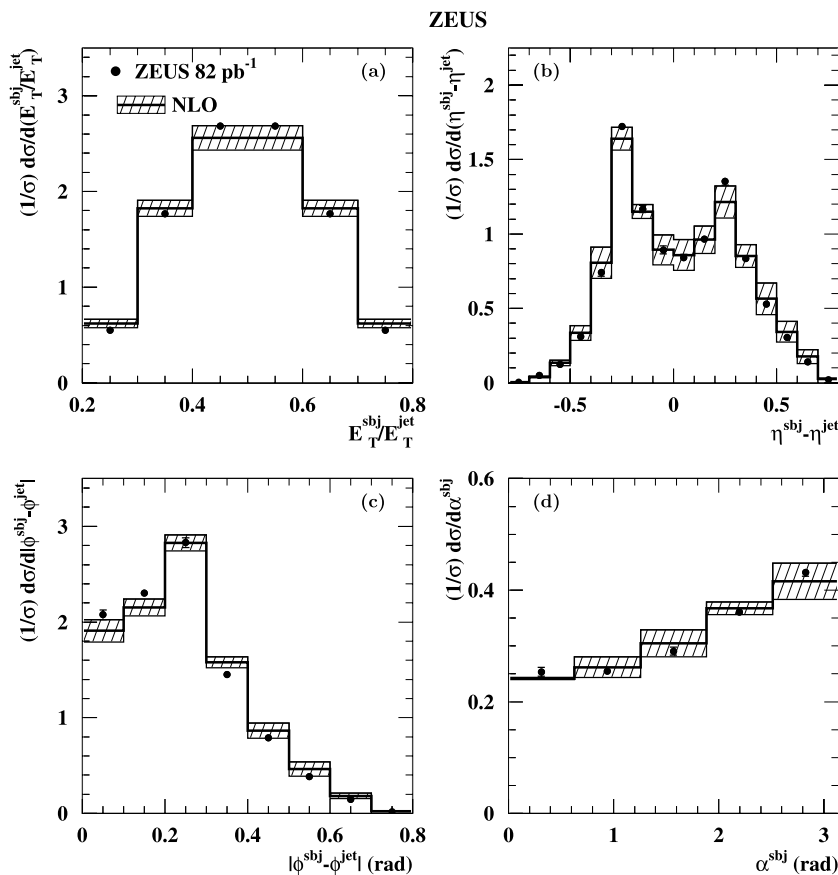
8.1 Comparison with NLO QCD calculations

Next-to-leading-order QCD calculations are compared to the data in Figs. 3 and 4. The QCD predictions give an adequate description of the data. However, the data points are situated at the upper (lower) edge of the theoretical uncertainty in some regions of the subjet variables such as $E_T^{sbj}/E_T^{jet} \sim 0.5$, $|\phi^{sbj} - \phi^{jet}| \sim 0$, $\alpha^{sbj} \sim 0$ and the peaks in the $\eta^{sbj} - \eta^{jet}$ distribution ($E_T^{sbj}/E_T^{jet} \sim 0.25$, $|\phi^{sbj} - \phi^{jet}| > 0.3$ and $|\eta^{sbj} - \eta^{jet}| > 0.5$). Since the calculations are normalized to unity, the uncertainties are correlated among the points; this correlation gives rise to the pulsating pattern exhibited by the theoretical uncertainties.

The calculation of the cross section as a function of E_T^{sbj}/E_T^{jet} exhibits a peak at $0.4 < E_T^{sbj}/E_T^{jet} < 0.6$, as seen in the data. The calculations for the $\eta^{sbj} - \eta^{jet}$ and α^{sbj} distributions predict that the subjet with higher transverse energy tends to be in the rear direction, in agreement with the data. This shows that the mechanism driving the subjet topology in the data is the $eq \to eqg$ and $eg \to eq\bar{q}$ subprocesses as implemented in the pQCD calculations.

To gain further insight into the pattern of parton radiation, the predictions for quark- and gluon-induced processes (see Sect. 2) are compared separately with the data in Fig. 5. The NLO calculations predict that the two-subjet rate is dominated by quark-induced processes: the relative contribution
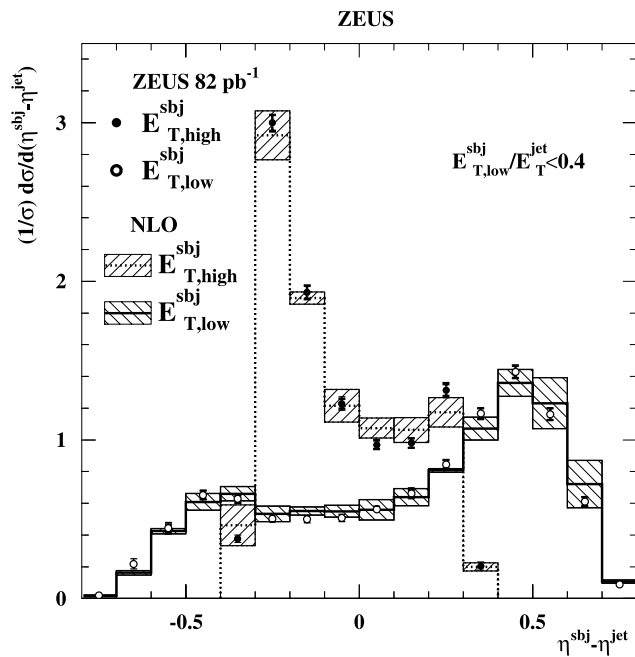
of quark- (gluon-) induced processes is 81% (19%). The shape of the predictions for these two types of processes are different; in quark-induced processes, the two subjets have more similar transverse energies (see Fig. 5a) and are closer to each other (see Fig. 5b and 5c) than in gluon-induced processes. The comparison with the measurements shows that the data are better described by the calculations for jets arising from a qg pair than those coming from a $q\bar{q}$ pair.

8.2 E_T^{jet}, Q^2 and x dependence of the subjet distributions

Figures 6, 7, 8, 9 show the normalized differential subjet cross sections in different regions of E_T^{jet}. Even though the mean subjet multiplicity decreases with increasing E_T^{jet} [19], the measured normalized differential subjet cross sections have very similar shapes in all E_T^{jet} regions for all the observables considered. This means that the subjet topology does not change significantly with E_T^{jet}. This is better illustrated in Fig. 10, where the data for all E_T^{jet} regions are plotted together. In particular, it is observed that the maximum of each measured normalized cross section in every region of E_T^{jet} occurs in the same bin of the distribution. To quantify the E_T^{jet} dependence more precisely, Fig. 11 shows the maximum value of the measured normalized cross section for each observable as a function of E_T^{jet} together with the NLO predictions. The spread of the measured maximum values of the normalized cross sections is $\pm(4$–$6)\%$. For each observable, the scaling behavior of the normalized differential subjet cross sections is clearly observed and in agreement with the expectation that the splitting functions depend weakly on the energy scale. The NLO QCD calculations are in agreement with the data and support this observation.

Figures 12, 13, 14, 15 show the normalized differential subjet cross sections in different regions of Q^2. In this case, it is observed that while the shape of the E_T^{sbj}/E_T^{jet} distribution does not change significantly with Q^2, some dependence can be seen in the other observables. For example, the dip in the $\eta^{sbj} - \eta^{jet}$ distribution is shallower for $125 < Q^2 < 250$ GeV^2 than at higher Q^2 and the shape of the α^{sbj} distribution for $125 < Q^2 < 250$ GeV^2 is somewhat different than for the other regions (see Fig. 16). These features of the data are reasonably reproduced by the NLO QCD calculations and understood as a combination of two effects: the fraction of gluon-induced events is predicted to be 32% for $125 < Q^2 < 250$ GeV^2 and below 14% for higher Q^2; the shape of the normalized cross sections as functions of $\eta^{sbj} - \eta^{jet}$ and α^{sbj} changes from the region $125 < Q^2 < 250$ GeV^2 to $250 < Q^2 < 500$ GeV^2 (see Fig. 17) for quark- and gluon-induced events. It is observed that the maximum of each measured normalized cross section in every region of Q^2 occurs in the same bin of the distribution, except for $|\phi^{sbj} - \phi^{jet}|$ in the highest-Q^2 region.
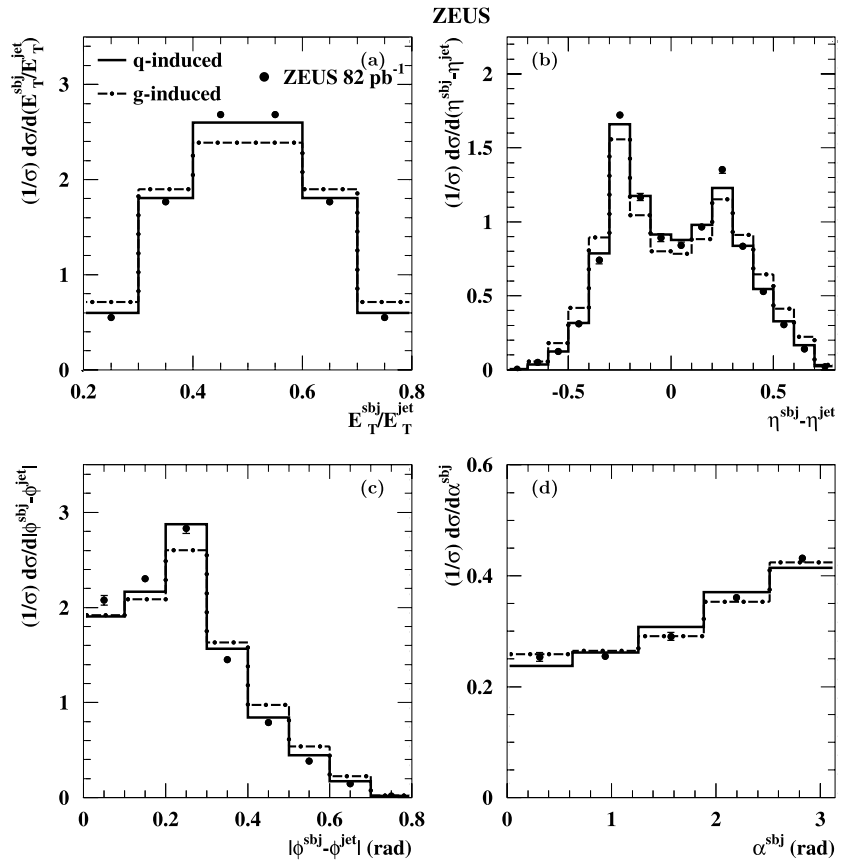

Fig. 4 Measured normalized differential subjet cross sections for jets with $E_T^{jet} > 14$ GeV and $-1 < \eta^{jet} < 2.5$ which have two subjets for $y_{cut} = 0.05$ in the kinematic region given by $Q^2 > 125$ GeV^2 and $E_{T,low}^{sbj}/E_T^{jet} < 0.4$ as functions of $\eta^{sbj} - \eta^{jet}$ separately for the higher (*dots*) and lower (*open circles*) E_T^{sbj} subjets. Other details are as in the caption to Fig. 3
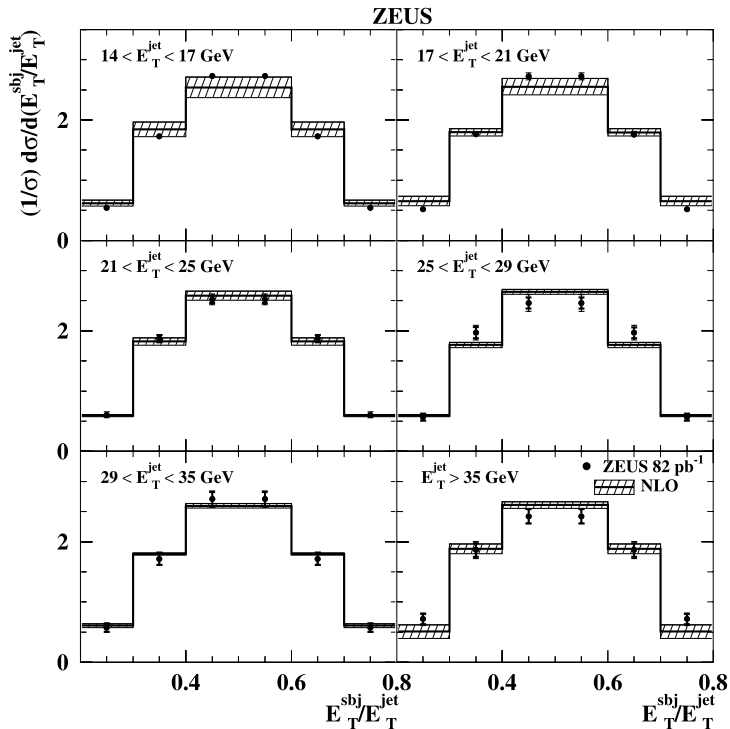
536

Eur. Phys. J. C (2009) 63: 527–548

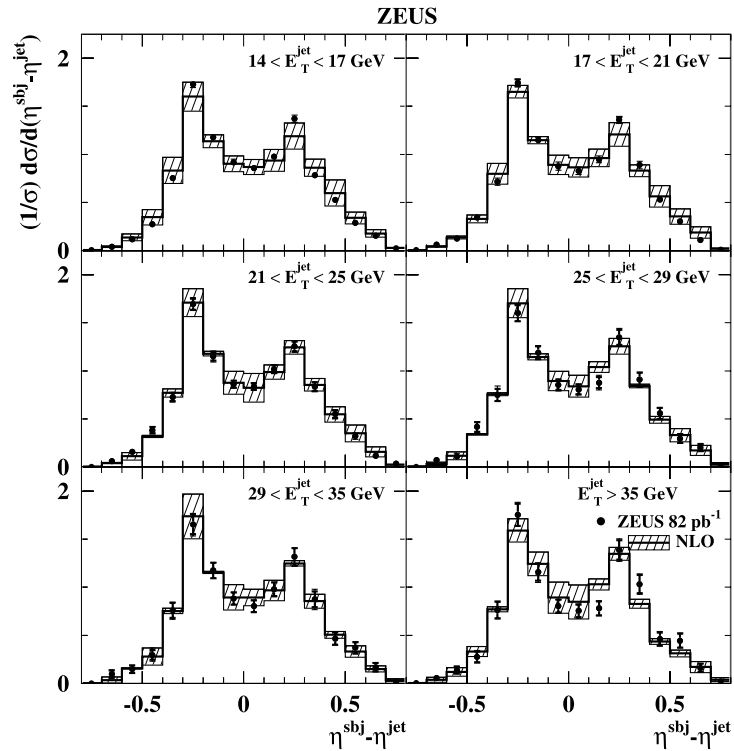**Fig. 5** Measured normalized differential subjet cross sections (*dots*) for jets with $E_T^{jet} > 14$ GeV and $-1 < \eta^{jet} < 2.5$ which have two subjets for $y_{cut} = 0.05$ in the kinematic region given by $Q^2 > 125$ GeV^2 as functions of (**a**) E_T^{sbj}/E_T^{jet}, (**b**) $\eta^{sbj} - \eta^{jet}$, (**c**) $|\phi^{sbj} - \phi^{jet}|$ and (**d**) α^{sbj}. For comparison, the NLO predictions for quark- (*solid histograms*) and gluon-induced (*dot-dashed histograms*) processes are included. Other details are as in the caption to Fig. 3

Fig. 6 Measured normalized differential subjet cross sections (*dots*) for jets with $E_T^{jet} > 14$ GeV and $-1 < \eta^{jet} < 2.5$ which have two subjets for $y_{cut} = 0.05$ in the kinematic region given by $Q^2 > 125$ GeV^2 as functions of E_T^{sbj}/E_T^{jet} in different regions of E_T^{jet}. Other details are as in the caption to Fig. 3
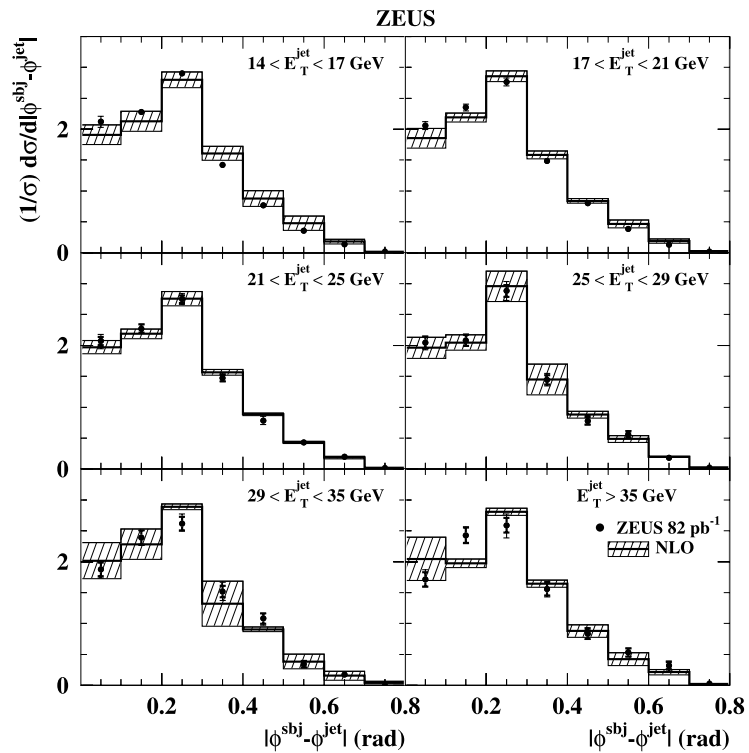
Fig. 7 Measured normalized differential subset cross sections (*dots*) for jets with $E_T^{jet} > 14$ GeV and $-1 < \eta^{jet} < 2.5$ which have two subjets for $y_{cut} = 0.05$ in the kinematic region given by $Q^2 > 125$ GeV^2 as functions of $\eta^{sbj} - \eta^{jet}$ in different regions of E_T^{jet}. Other details are as in the caption to Fig. 3

Fig. 8 Measured normalized differential subset cross sections (*dots*) for jets with $E_T^{jet} > 14$ GeV and $-1 < \eta^{jet} < 2.5$ which have two subjets for $y_{cut} = 0.05$ in the kinematic region given by $Q^2 > 125$ GeV^2 as functions of $|\phi^{sbj} - \phi^{jet}|$ in different regions of E_T^{jet}. Other details are as in the caption to Fig. 3

538

Eur. Phys. J. C (2009) 63: 527–548

Fig. 9 Measured normalized differential subjet cross sections (*dots*) for jets with $E_T^{jet} > 14$ GeV and $-1 < \eta^{jet} < 2.5$ which have two subjets for $y_{cut} = 0.05$ in the kinematic region given by $Q^2 > 125$ GeV^2 as functions of α^{sbj} in different regions of E_T^{jet}. Other details are as in the caption to Fig. 3
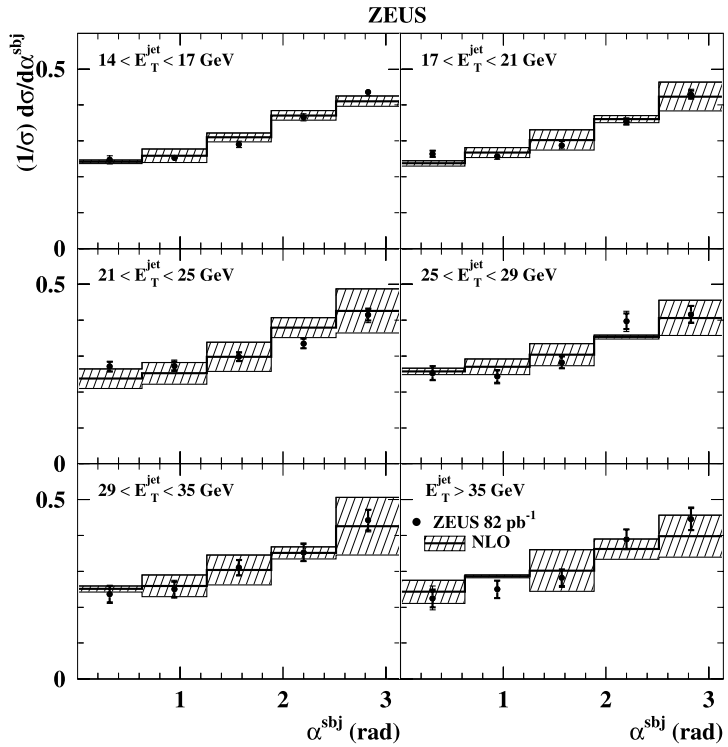

Fig. 10 Measured normalized differential subjet cross sections for jets with $E_T^{jet} > 14$ GeV and $-1 < \eta^{jet} < 2.5$ which have two subjets for $y_{cut} = 0.05$ in the kinematic region given by $Q^2 > 125$ GeV^2 as functions of (**a**) E_T^{sbj}/E_T^{jet}, (**b**) $\eta^{sbj} - \eta^{jet}$, (**c**) $|\phi^{sbj} - \phi^{jet}|$ and (**d**) α^{sbj} in different regions of E_T^{jet}. Details concerning the error bars are as in the caption to Fig. 3
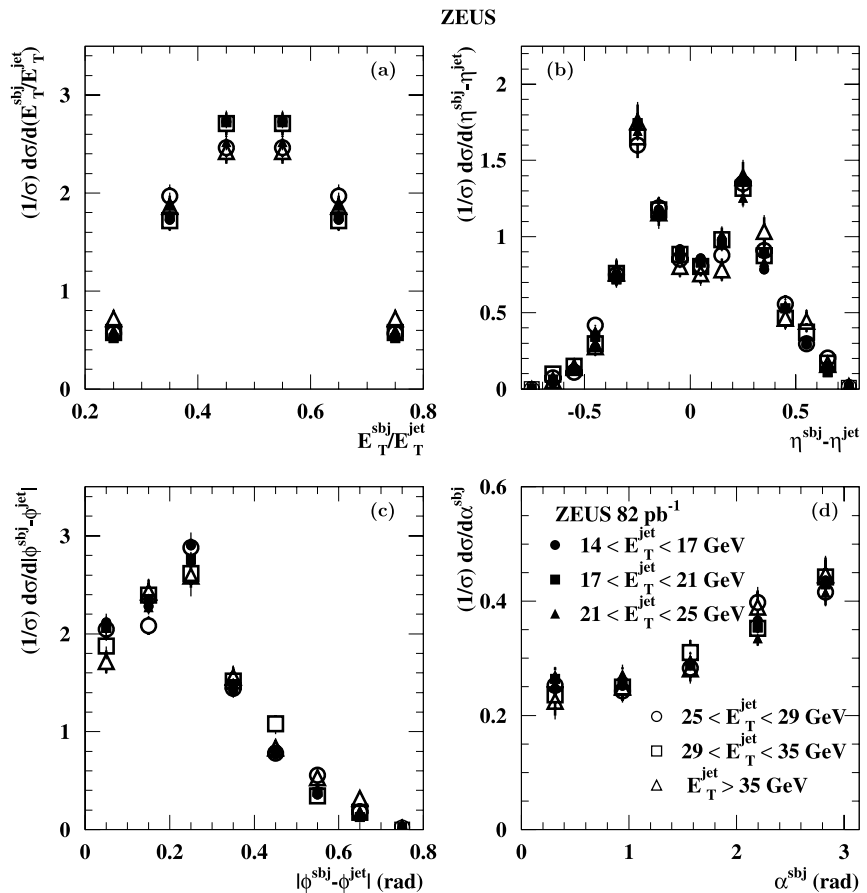
Fig. 11 Maximum of the measured normalized differential (**a**) E_T^{sbj}/E_T^{jet}, (**b**) $\eta^{sbj} - \eta^{jet}$, (**c**) $|\phi^{sbj} - \phi^{jet}|$ and (**d**) α^{sbj} subject cross sections (*dots*) for jets with $E_T^{jet} > 14$ GeV and $-1 < \eta^{jet} < 2.5$ which have two subjets for $y_{cut} = 0.05$ in the kinematic region given by $Q^2 > 125$ GeV^2 as a function of E_T^{jet}. For comparison, the NLO predictions for quark- (*dotted histograms*) and gluon-induced (*dot-dashed histograms*) processes are also shown separately. Other details are as in the caption to Fig. 3
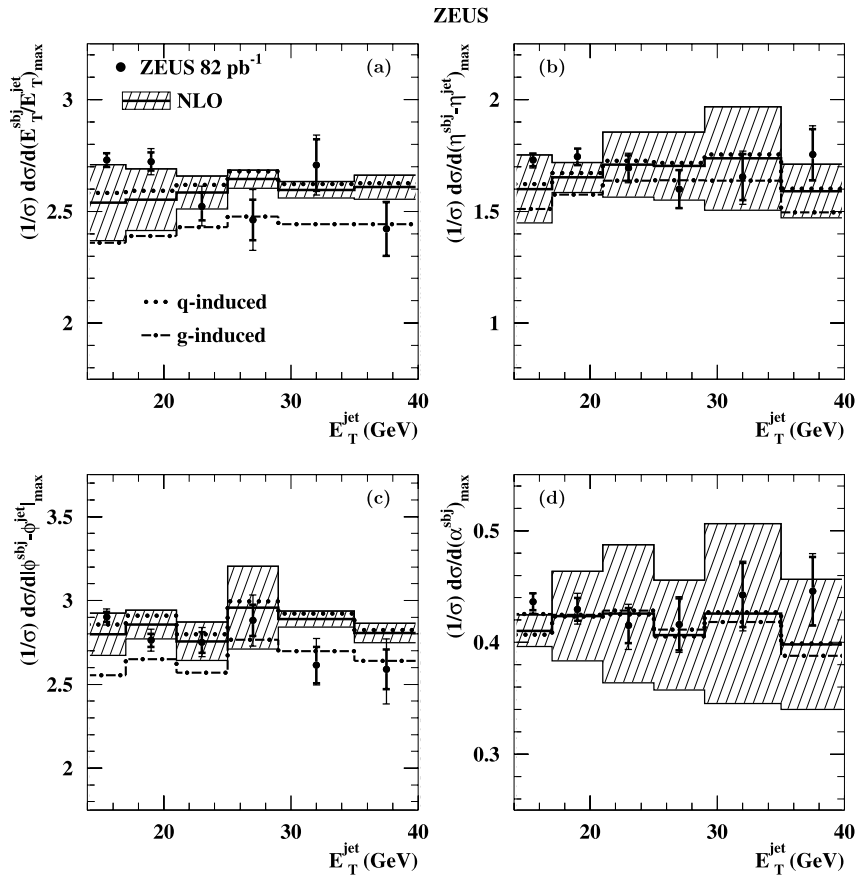

Fig. 12 Measured normalized differential subject cross sections (*dots*) for jets with $E_T^{jet} > 14$ GeV and $-1 < \eta^{jet} < 2.5$ which have two subjets for $y_{cut} = 0.05$ in the kinematic region given by $Q^2 > 125$ GeV^2 as functions of E_T^{sbj}/E_T^{jet} in different regions of Q^2. For comparison, the LO QCD predictions (*dashed histograms*) are included. Other details are as in the caption to Fig. 3
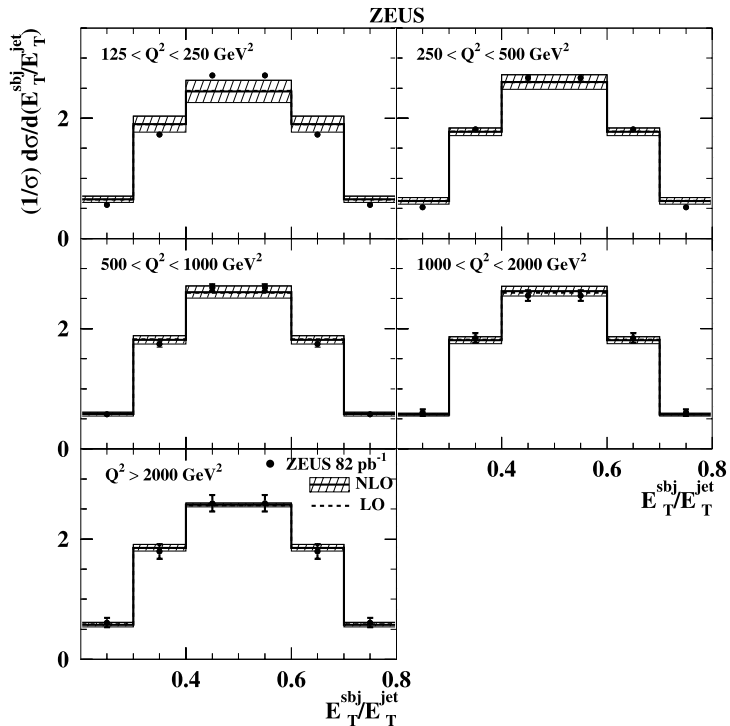
540

Eur. Phys. J. C (2009) 63: 527–548

Fig. 13 Measured normalized differential subjet cross sections (*dots*) for jets with $E_T^{jet} > 14$ GeV and $-1 < \eta^{jet} < 2.5$ which have two subjets for $y_{cut} = 0.05$ in the kinematic region given by $Q^2 > 125$ GeV^2 as functions of $\eta^{sbj} - \eta^{jet}$ in different regions of Q^2. Other details are as in the caption to Fig. 12

Fig. 14 Measured normalized differential subjet cross sections (*dots*) for jets with $E_T^{jet} > 14$ GeV and $-1 < \eta^{jet} < 2.5$ which have two subjets for $y_{cut} = 0.05$ in the kinematic region given by $Q^2 > 125$ GeV^2 as functions of $|\phi^{sbj} - \phi^{jet}|$ in different regions of Q^2. Other details are as in the caption to Fig. 12

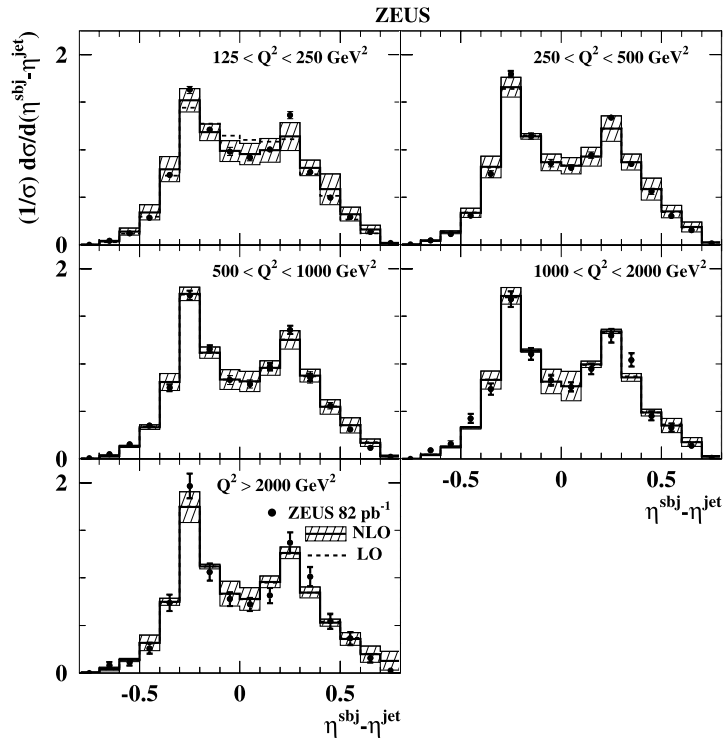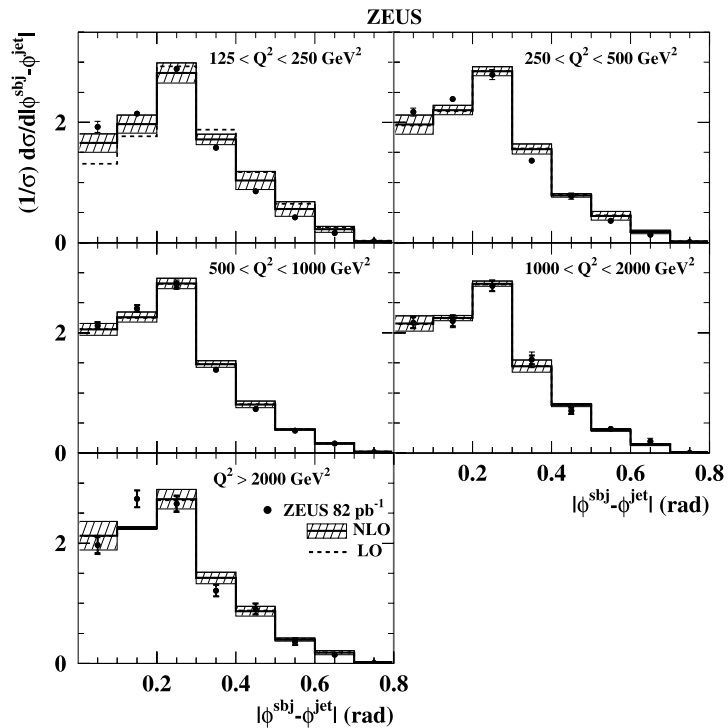**Fig. 15** Measured normalized differential subject cross sections (*dots*) for jets with $E_T^{\text{jet}} > 14$ GeV and $-1 < \eta^{\text{jet}} < 2.5$ which have two subjets for $y_{\text{cut}} = 0.05$ in the kinematic region given by $Q^2 > 125$ GeV^2 as functions of α^{sbj} in different regions of Q^2. Other details are as in the caption to Fig. 12
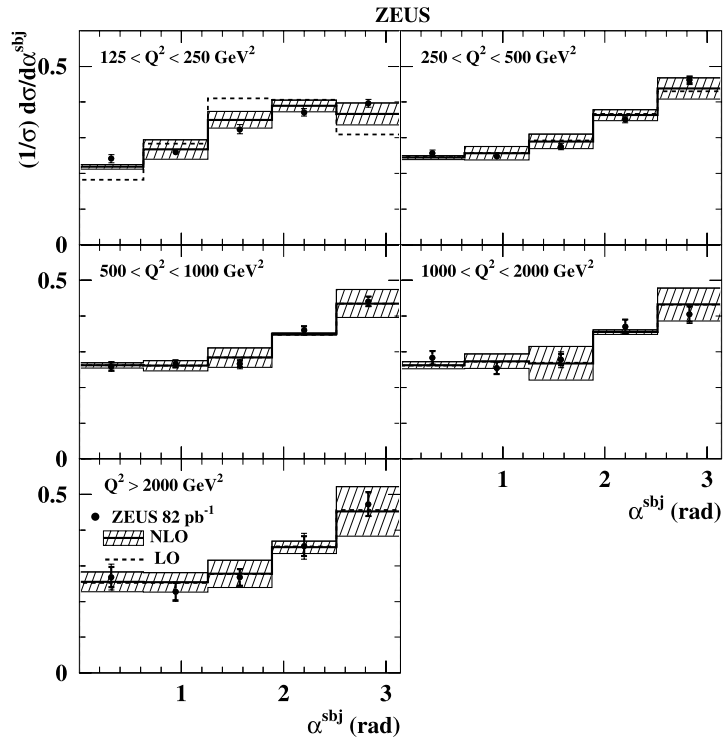

Fig. 16 Measured normalized differential subject cross sections for jets with $E_T^{\text{jet}} > 14$ GeV and $-1 < \eta^{\text{jet}} < 2.5$ which have two subjets for $y_{\text{cut}} = 0.05$ in the kinematic region given by $Q^2 > 125$ GeV^2 as functions of (**a**) $E_T^{\text{sbj}}/E_T^{\text{jet}}$, (**b**) $\eta^{\text{sbj}} - \eta^{\text{jet}}$, (**c**) $|\phi^{\text{sbj}} - \phi^{\text{jet}}|$ and (**d**) α^{sbj} in different regions of Q^2. Details concerning the error bars are as in the caption to Fig. 3
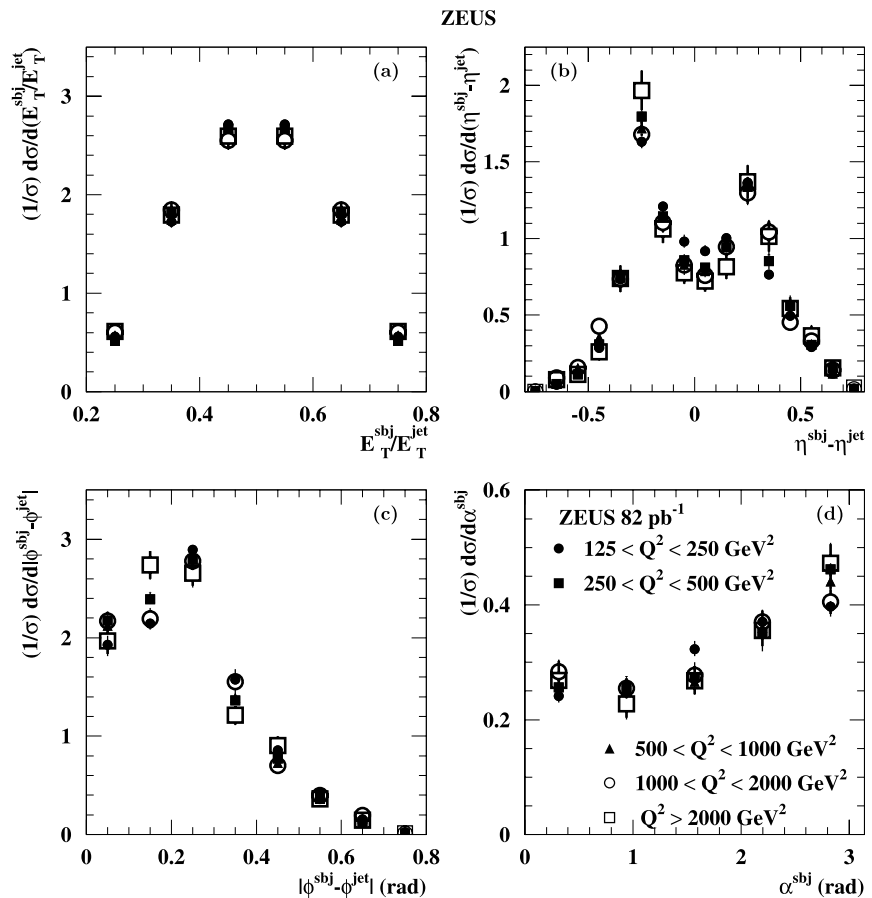
Fig. 17 Predicted normalized differential subjet cross sections (*solid histograms*) for jets with $E_T^{\text{jet}} > 14$ GeV and $-1 < \eta^{\text{jet}} < 2.5$ which have two subjets for $y_{\text{cut}} = 0.05$ in the kinematic region given by $Q^2 > 125$ GeV^2 as functions of (**a, c**) $\eta^{\text{sbj}} - \eta^{\text{jet}}$ and (**b, d**) α^{sbj} in different regions of Q^2. The NLO predictions for quark- (*dotted histograms*) and gluon-induced (*dot-dashed histograms*) processes are also shown separately
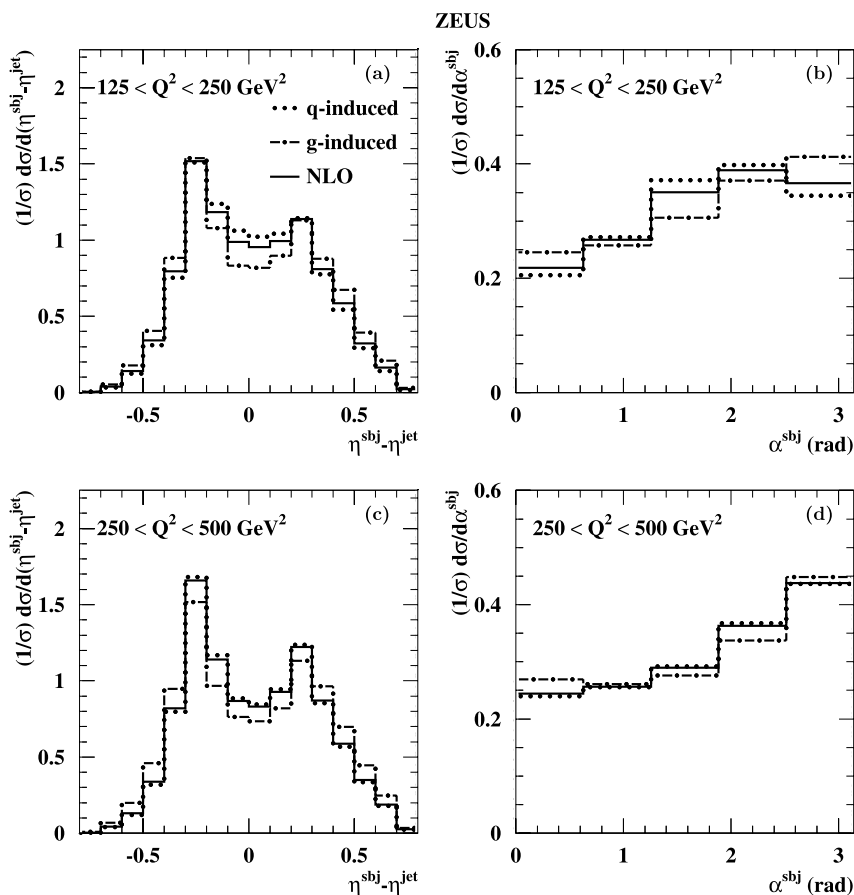

Figure 18 shows the maximum[4] value of the measured normalized cross section for each observable as a function of Q^2 together with the NLO predictions. The spread of the measured maximum values of the normalized cross sections as functions of $E_T^{\text{sbj}}/E_T^{\text{jet}}$ and $|\phi^{\text{sbj}} - \phi^{\text{jet}}|$ is $\pm(3\text{–}4)\%$. On the other hand, the measured and predicted maximum values for the normalized cross sections as functions of $\eta^{\text{sbj}} - \eta^{\text{jet}}$ and α^{sbj} exhibit a step-like behavior between the lowest-Q^2 region and the rest.

Figures 19, 20, 21, 22 show the normalized differential subjet cross sections in different regions of x. It should be noted that due to HERA kinematics, the regions in x and Q^2 are correlated to some extent. Figure 23 shows the data for all x regions plotted together. It is observed that the maximum of each measured normalized cross section in every region of x occurs in the same bin of the distribution, except for $|\phi^{\text{sbj}} - \phi^{\text{jet}}|$ in the highest x region. Figure 24 shows the maximum[4] value of the measured normalized cross section for each observable as a function of x. The shape of the $E_T^{\text{sbj}}/E_T^{\text{jet}}$ measured distribution does not change significantly with x, whereas some dependence is expected (see

Fig. 24a). The dependence of the $\eta^{\text{sbj}} - \eta^{\text{jet}}$ and α^{sbj} distributions with x exhibits features similar to those observed in the study of the Q^2 dependence; in particular, the maximum values (see Figs. 24b and 24d) exhibit a monotonic increase as x increases, which is reasonably reproduced by the calculations. As discussed previously, these features are understood as a combination of two effects: a decrease of the predicted fraction of gluon-induced events from 44% for $0.004 < x < 0.009$ to 6% for $x > 0.093$ and the change in shape of the normalized cross sections for quark- and gluon-induced processes as x increases (see Fig. 25).

To investigate the origin of the change in shape of the normalized differential cross sections between the lowest and higher Q^2 and x regions, LO and NLO calculations were compared. The most dramatic change is observed when restricting the kinematic region to $125 < Q^2 < 250$ GeV^2 or $0.004 < x < 0.009$ (see Figs. 12 to 15 and Figs. 19 to 22); the LO calculation of the $\eta^{\text{sbj}} - \eta^{\text{jet}}$ distribution does not exhibit a two-peak structure as seen in the NLO prediction and in the data (see Figs. 13 and 20). In addition, the LO calculation of the α^{sbj} distribution peaks at $\alpha^{\text{sbj}} \sim \pi/2$ in contrast with the NLO prediction and the data (see Figs. 15 and 22). This proves that the NLO QCD radiative corrections are responsible for these variations in shape and necessary for describing the data.

---

[4]For the $|\phi^{\text{sbj}} - \phi^{\text{jet}}|$ distribution, the same bin has been used for consistency.

Eur. Phys. J. C (2009) 63: 527–548

543

Fig. 18 Maximum of the measured normalized differential (**a**) E_T^{sbj}/E_T^{jet}, (**b**) $\eta^{sbj} - \eta^{jet}$, (**c**) $|\phi^{sbj} - \phi^{jet}|$ and (**d**) α^{sbj} subject cross sections (*dots*) for jets with $E_T^{jet} > 14$ GeV and $-1 < \eta^{jet} < 2.5$ which have two subjets for $y_{cut} = 0.05$ in the kinematic region given by $Q^2 > 125$ GeV^2 as a function of Q^2. For comparison, the NLO predictions for quark- (*dotted histograms*) and gluon-induced (*dot-dashed histograms*) processes are also shown separately. Other details are as in the caption to Fig. 3
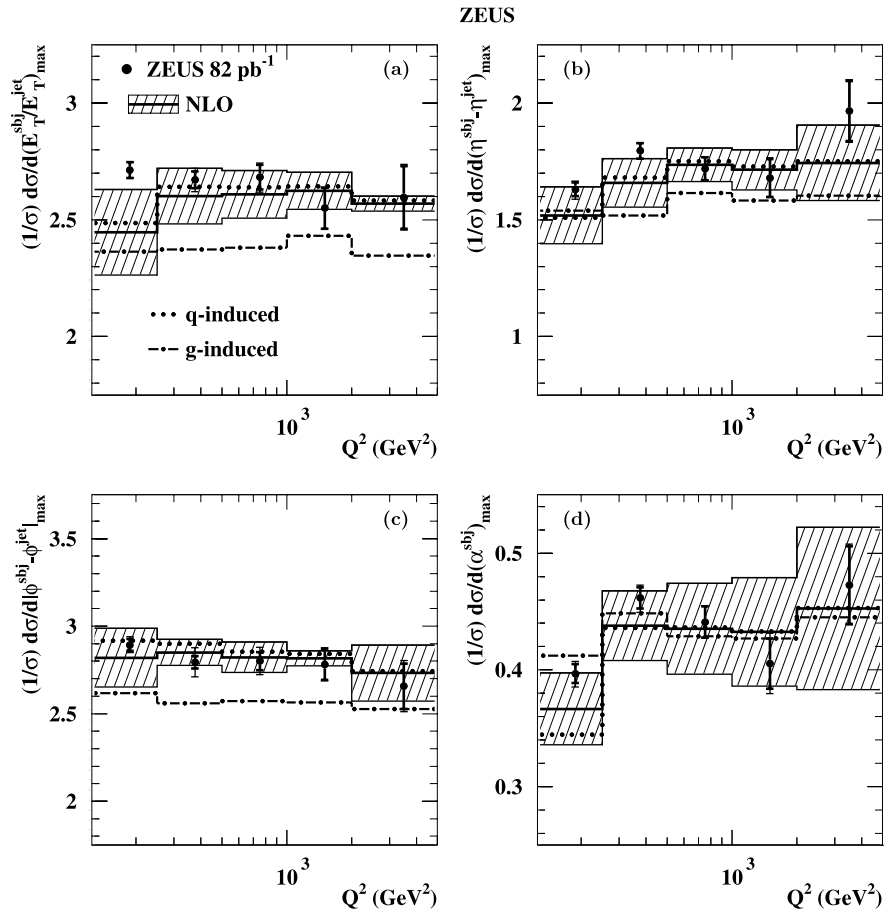

Fig. 19 Measured normalized differential subjet cross sections (*dots*) for jets with $E_T^{jet} > 14$ GeV and $-1 < \eta^{jet} < 2.5$ which have two subjets for $y_{cut} = 0.05$ in the kinematic region given by $Q^2 > 125$ GeV^2 as functions of E_T^{sbj}/E_T^{jet} in different regions of x. Other details are as in the caption to Fig. 12
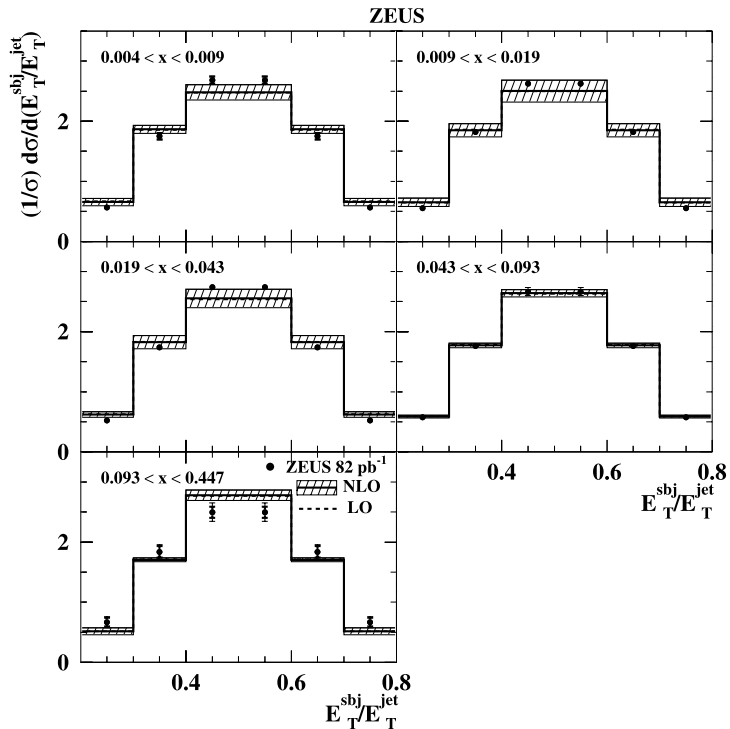
544

Eur. Phys. J. C (2009) 63: 527–548

Fig. 20 Measured normalized differential subjet cross sections (*dots*) for jets with $E_T^{\text{jet}} > 14$ GeV and $-1 < \eta^{\text{jet}} < 2.5$ which have two subjets for $y_{\text{cut}} = 0.05$ in the kinematic region given by $Q^2 > 125$ GeV^2 as functions of $\eta^{\text{sbj}} - \eta^{\text{jet}}$ in different regions of x. Other details are as in the caption to Fig. 12
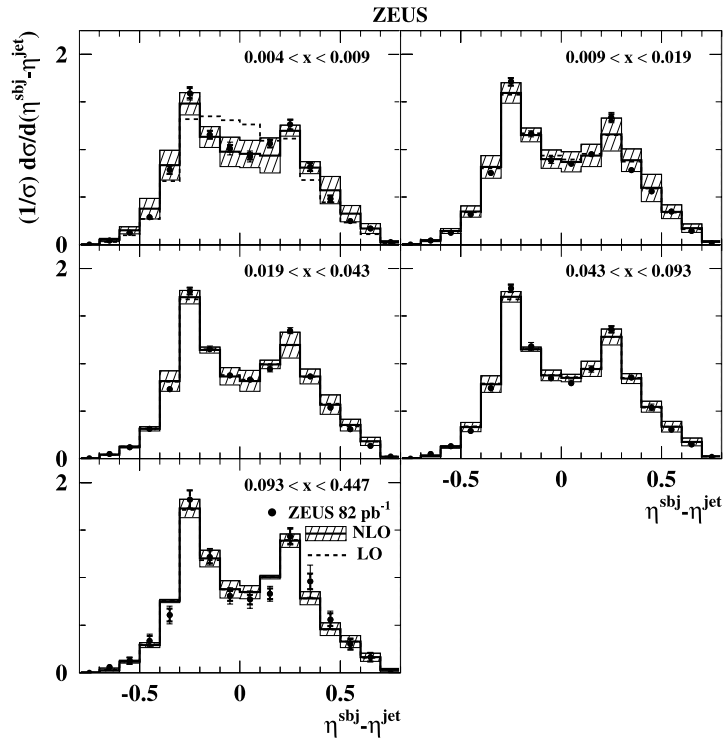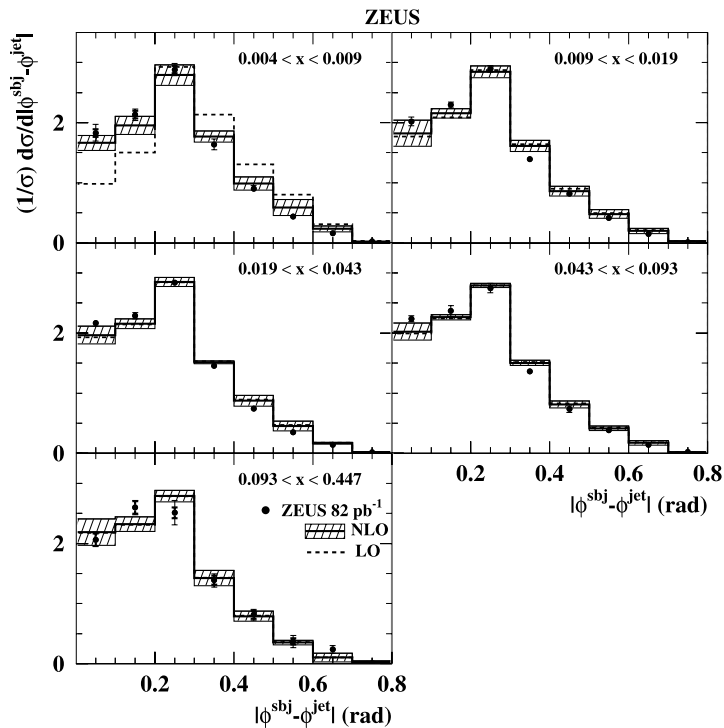

Fig. 21 Measured normalized differential subjet cross sections (*dots*) for jets with $E_T^{\text{jet}} > 14$ GeV and $-1 < \eta^{\text{jet}} < 2.5$ which have two subjets for $y_{\text{cut}} = 0.05$ in the kinematic region given by $Q^2 > 125$ GeV^2 as functions of $|\phi^{\text{sbj}} - \phi^{\text{jet}}|$ in different regions of x. Other details are as in the caption to Fig. 12

In summary, while the shapes of the normalized differential cross sections show only a weak dependence on E_T^{jet}, their dependence on Q^2 and x have some prominent features at low Q^2 or x. The weak dependence on E_T^{jet} is consistent with the expected scaling behavior of the splitting functions; however, the restriction to low Q^2 or x values demonstrates that the NLO QCD radiative corrections are important there. The NLO QCD calculations, which include

Fig. 22 Measured normalized differential subjet cross sections (*dots*) for jets with $E_T^{jet} > 14$ GeV and $-1 < \eta^{jet} < 2.5$ which have two subjets for $y_{cut} = 0.05$ in the kinematic region given by $Q^2 > 125$ GeV^2 as functions of α^{sbj} in different regions of x. Other details are as in the caption to Fig. 12

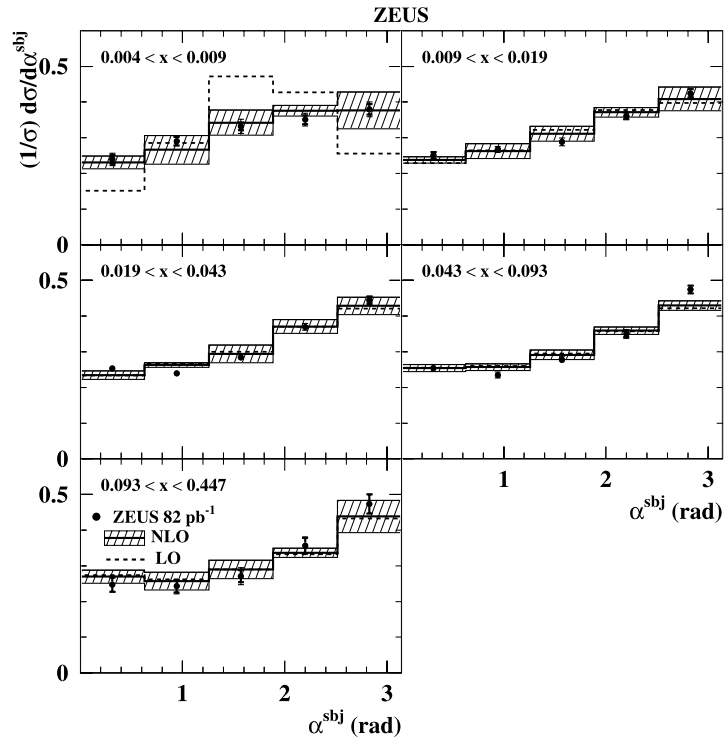**Fig. 23** Measured normalized differential subjet cross sections for jets with $E_T^{jet} > 14$ GeV and $-1 < \eta^{jet} < 2.5$ which have two subjets for $y_{cut} = 0.05$ in the kinematic region given by $Q^2 > 125$ GeV^2 as functions of (**a**) E_T^{sbj}/E_T^{jet}, (**b**) $\eta^{sbj} - \eta^{jet}$, (**c**) $|\phi^{sbj} - \phi^{jet}|$ and (**d**) α^{sbj} in different regions of x. Details concerning the error bars are as in the caption to Fig. 3
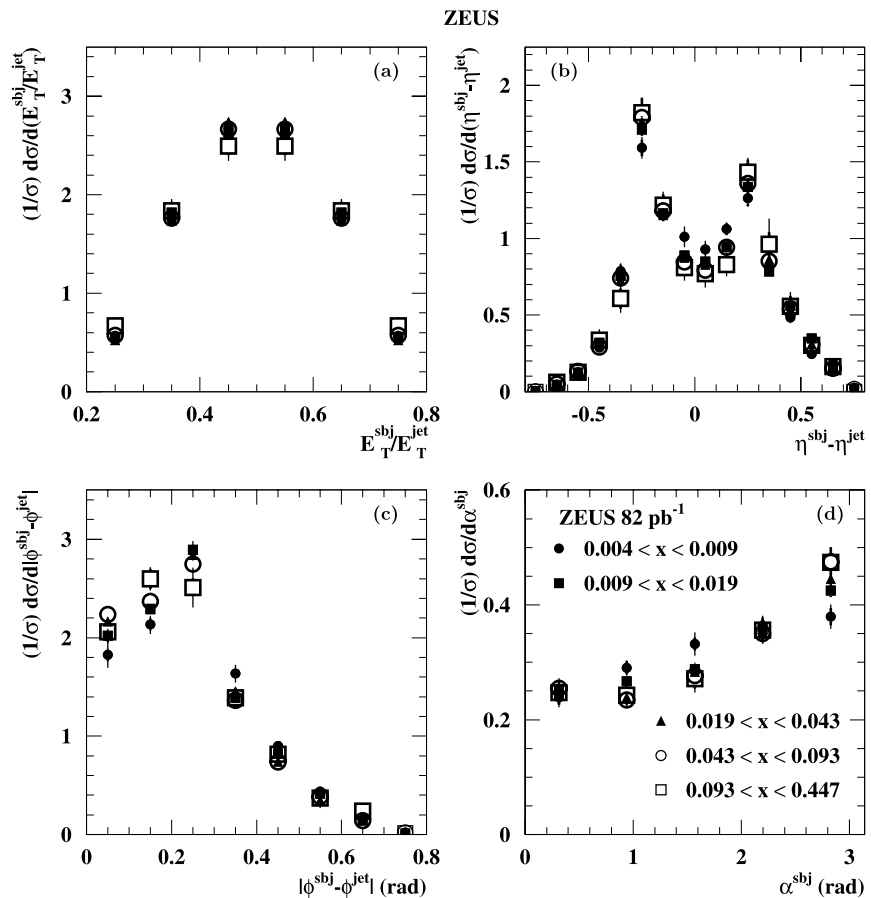
546

Eur. Phys. J. C (2009) 63: 527–548

Fig. 24 Maximum of the measured normalized differential (**a**) E_T^{sbj}/E_T^{jet}, (**b**) $\eta^{sbj} - \eta^{jet}$, (**c**) $|\phi^{sbj} - \phi^{jet}|$ and (**d**) α^{sbj} subjet cross sections (dots) for jets with $E_T^{jet} > 14$ GeV and $-1 < \eta^{jet} < 2.5$ which have two subjets for $y_{cut} = 0.05$ in the kinematic region given by $Q^2 > 125$ GeV^2 as a function of x. For comparison, the NLO predictions for quark- (*dotted histograms*) and gluon-induced (*dot-dashed histograms*) processes are also shown separately. Other details are as in the caption to Fig. 3
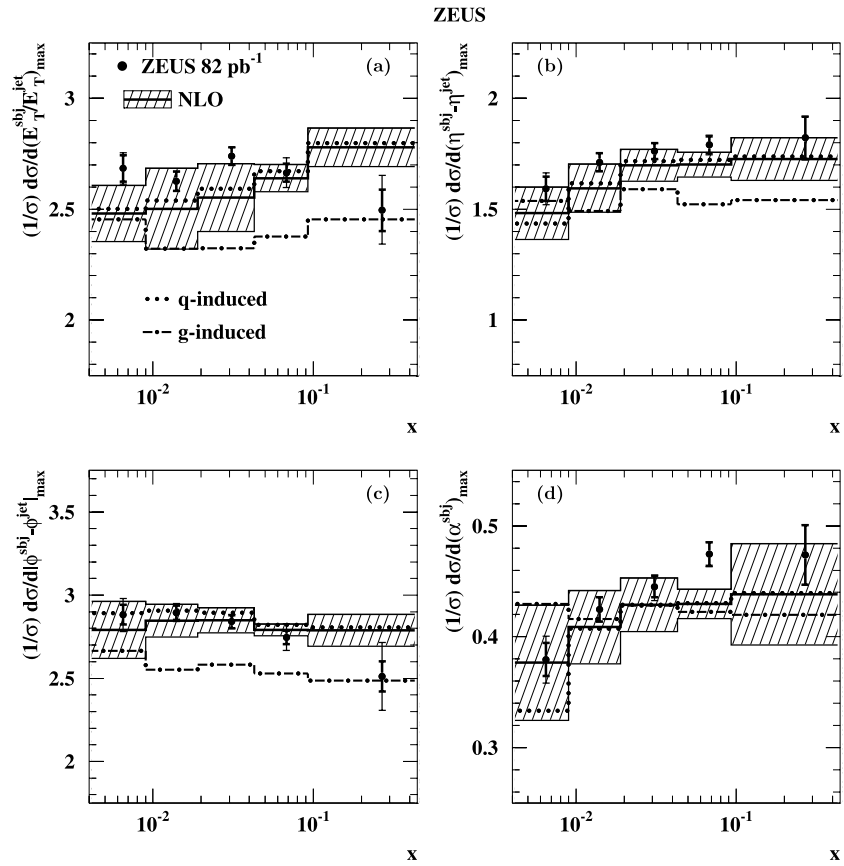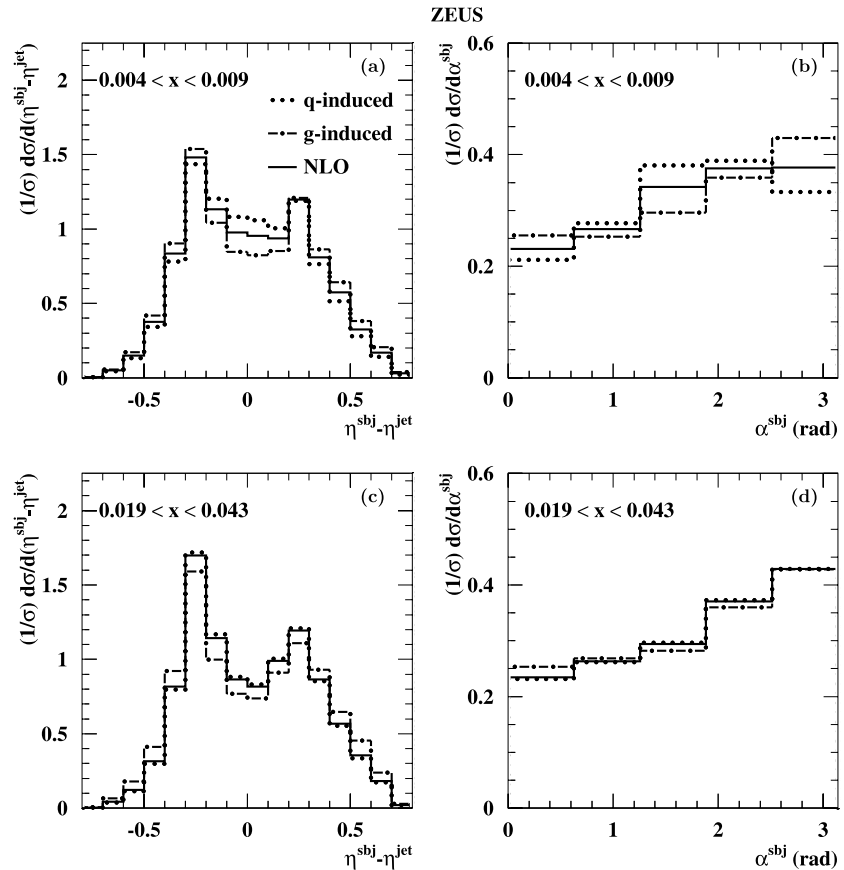

Fig. 25 Predicted normalized differential subjet cross sections (*solid histograms*) for jets with $E_T^{jet} > 14$ GeV and $-1 < \eta^{jet} < 2.5$ which have two subjets for $y_{cut} = 0.05$ in the kinematic region given by $Q^2 > 125$ GeV^2 as functions of (**a**, **c**) $\eta^{sbj} - \eta^{jet}$ and (**b**, **d**) α^{sbj} in different regions of x. The NLO predictions for quark- (*dotted histograms*) and gluon-induced (*dot-dashed histograms*) processes are also shown separately

the two competing processes $eq \rightarrow eqg$ and $eg \rightarrow eq\bar{q}$ and radiative corrections, adequately reproduce the measurements.

9 Summary

Normalized differential subjet cross sections in inclusive-jet NC DIS were measured in ep collisions using 81.7 pb^{-1} of data collected with the ZEUS detector at HERA. The cross sections refer to jets identified in the laboratory frame with the k_T cluster algorithm in the longitudinally invariant inclusive mode and selected with $E_T^{\mathrm{jet}} > 14$ GeV and $-1 < \eta^{\mathrm{jet}} < 2.5$. The measurements were made for those jets which have exactly two subjets for $y_{\mathrm{cut}} = 0.05$ in the kinematic region defined by $Q^2 > 125$ GeV^2.

The cross sections were measured as functions of $E_T^{\mathrm{sbj}}/E_T^{\mathrm{jet}}$, $\eta^{\mathrm{sbj}} - \eta^{\mathrm{jet}}$, $|\phi^{\mathrm{sbj}} - \phi^{\mathrm{jet}}|$ and α^{sbj}. The data show that the two subjets tend to have similar transverse energies and that the subjet with higher transverse energy tends to be in the rear direction. This is consistent with the effects of color coherence between the initial and final states, which predict that soft parton radiation is emitted predominantly towards the proton beam direction.

An adequate description of the data is given by NLO QCD calculations. This means that the pattern of parton radiation as predicted by QCD reproduces the subjet topology in the data. Furthermore, the subjet distributions in the data are better described by the calculations for jets arising from a quark-gluon pair.

The normalized cross sections show a weak dependence on E_T^{jet}, in agreement with the expected scaling behavior of the splitting functions. By restricting the measurements to low Q^2 or x values, significant differences in shape are observed, which can be primarily attributed to NLO QCD radiative corrections.

References

1. S. Chekanov et al. (ZEUS Collaboration), Phys. Lett. B **531**, 9 (2002)
2. S. Chekanov et al. (ZEUS Collaboration), Eur. Phys. J. C **23**, 615 (2002)
3. J. Breitweg et al. (ZEUS Collaboration), Phys. Lett. B **443**, 394 (1998)
4. J. Breitweg et al. (ZEUS Collaboration), Phys. Lett. B **507**, 70 (2001)
5. S. Chekanov et al. (ZEUS Collaboration), Phys. Lett. B **547**, 164 (2002)
6. S. Chekanov et al. (ZEUS Collaboration), Eur. Phys. J. C **23**, 13 (2002)
7. S. Chekanov et al. (ZEUS Collaboration), Phys. Lett. B **560**, 7 (2003)
8. S. Chekanov et al. (ZEUS Collaboration), Eur. Phys. J. C **31**, 149 (2003)
9. S. Chekanov et al. (ZEUS Collaboration), Nucl. Phys. B **765**, 1 (2007)
10. S. Chekanov et al. (ZEUS Collaboration), Phys. Lett. B **649**, 12 (2007)
11. C. Adloff et al. (H1 Collaboration), Phys. Lett. B **515**, 17 (2001)
12. C. Adloff et al. (H1 Collaboration), Eur. Phys. J. C **19**, 289 (2001)
13. C. Adloff et al. (H1 Collaboration), Eur. Phys. J. C **19**, 429 (2001)
14. C. Adloff et al. (H1 Collaboration), Eur. Phys. J. C **25**, 13 (2002)
15. C. Adloff et al. (H1 Collaboration), Phys. Lett. B **542**, 193 (2002)
16. C. Adloff et al. (H1 Collaboration), Eur. Phys. J. C **29**, 497 (2003)
17. A. Aktas et al. (H1 Collaboration), Phys. Lett. B **639**, 21 (2006)
18. A. Aktas et al. (H1 Collaboration), Phys. Lett. B **653**, 134 (2007)
19. S. Chekanov et al. (ZEUS Collaboration), Phys. Lett. B **558**, 41 (2003)
20. S. Chekanov et al. (ZEUS Collaboration), Nucl. Phys. B **700**, 3 (2004)
21. J. Thaler, L.-T. Wang, J. High Energy Phys. **0807**, 092 (2008)
22. D.E. Kaplan et al., Preprint, arXiv:0806.0848 (2008)
23. J.M. Butterworth et al., Phys. Rev. Lett. **100**, 242001 (2008)
24. S. Catani et al., Nucl. Phys. B **406**, 187 (1993)
25. S.D. Ellis, D.E. Soper, Phys. Rev. D **48**, 3160 (1993)
26. S. Catani et al., Nucl. Phys. B **383**, 419 (1992)
27. M.H. Seymour, Nucl. Phys. B **421**, 545 (1994)
28. M.H. Seymour, Phys. Lett. B **378**, 279 (1996)
29. J.R. Forshaw, M.H. Seymour, J. High Energy Phys. **9909**, 009 (1999)
30. F. Abe et al. (CDF Collaboration), Phys. Rev. D **50**, 5562 (1994)
31. M. Derrick et al. (ZEUS Collaboration), Phys. Lett. B **293**, 465 (1992)
32. U. Holm (ed.) (ZEUS Collaboration), *The ZEUS Detector*. Status Report (unpublished), DESY (1993). Available on http://www-zeus.desy.de/bluebook/bluebook.html
33. N. Harnew et al., Nucl. Instrum. Methods A **279**, 290 (1989)
34. B. Foster et al., Nucl. Phys. Proc. Suppl. B **32**, 181 (1993)
35. B. Foster et al., Nucl. Instrum. Methods A **338**, 254 (1994)
36. M. Derrick et al., Nucl. Instrum. Methods A **309**, 77 (1991)
37. A. Andresen et al., Nucl. Instrum. Methods A **309**, 101 (1991)
38. A. Caldwell et al., Nucl. Instrum. Methods A **321**, 356 (1992)
39. A. Bernstein et al., Nucl. Instrum. Methods A **336**, 23 (1993)
40. J. Andruszków et al., Preprint DESY-92-066, DESY (1992)
41. M. Derrick et al. (ZEUS Collaboration), Z. Phys. C **63**, 391 (1994)
42. J. Andruszków et al., Acta Phys. Pol. B **32**, 2025 (2001)
43. H. Abramowicz, A. Caldwell, R. Sinkus, Nucl. Instrum. Methods A **365**, 508 (1995)
44. R. Sinkus, T. Voss, Nucl. Instrum. Methods A **391**, 360 (1997)
45. S. Bentvelsen, J. Engelen, P. Kooijman, in *Proc. of the Workshop on Physics at HERA*, ed. by W. Buchmüller, G. Ingelman, vol. 1. Hamburg, Germany, DESY (1992), p. 23
46. K.C. Höger, in *Proc. of the Workshop on Physics at HERA*, ed. by W. Buchmüller, G. Ingelman, vol. 1. Hamburg, Germany, DESY (1992), p. 43
47. R. Brun et al., GEANT3, Technical Report CERN-DD/EE/84-1, CERN (1987)
48. A. Kwiatkowski, H. Spiesberger, H.-J. Möhring, Comput. Phys. Commun. **69**, 155 (1992)

548

Eur. Phys. J. C (2009) 63: 527–548

49. H. Spiesberger, *An Event Generator for ep Interactions at HERA Including Radiative Processes (Version 4.6)* (1996). Available on http://www.desy.de/~hspiesb/heracles.html

50. K. Charchuła, G.A. Schuler, H. Spiesberger, Comput. Phys. Commun. **81**, 381 (1994)

51. H. Spiesberger, HERACLES and DJANGOH: *Event Generation for ep Interactions at HERA Including Radiative Processes* (1998). Available on http://www.thep.physik.uni-mainz.de/~hspiesb/djangoh/djangoh.html

52. Y. Azimov et al., Phys. Lett. B **165**, 147 (1985)

53. G. Gustafson, Phys. Lett. B **175**, 453 (1986)

54. G. Gustafson, U. Pettersson, Nucl. Phys. B **306**, 746 (1988)

55. B. Andersson et al., Z. Phys. C **43**, 625 (1989)

56. L. Lönnblad, Comput. Phys. Commun. **71**, 15 (1992)

57. L. Lönnblad, Z. Phys. C **65**, 285 (1995)

58. G. Ingelman, A. Edin, J. Rathsman, Comput. Phys. Commun. **101**, 108 (1997)

59. H.L. Lai et al., Eur. Phys. J. C **12**, 375 (2000)

60. B. Andersson et al., Phys. Rep. **97**, 31 (1983)

61. T. Sjöstrand, Comput. Phys. Commun. **82**, 74 (1994)

62. T. Sjöstrand et al., Comput. Phys. Commun. **135**, 238 (2001)

63. T. Sjöstrand, Comput. Phys. Commun. **39**, 347 (1986)

64. T. Sjöstrand, M. Bengtsson, Comput. Phys. Commun. **43**, 367 (1987)

65. S. Catani, M.H. Seymour, Nucl. Phys. B **485**, 291 (1997). Erratum in Nucl. Phys. B **510**, 503 (1998)

66. R.K. Ellis, D.A. Ross, A.E. Terrano, Nucl. Phys. B **178**, 421 (1981)

67. S. Chekanov et al. (ZEUS Collaboration), Phys. Rev. D **67**, 012007 (2003)

68. Z. Nagy, Z. Trocsanyi, Phys. Rev. Lett. **87**, 082001 (2001)

69. G. Marchesini et al., Comput. Phys. Commun. **67**, 465 (1992)

70. G. Corcella et al., J. High Energy Phys. **0101**, 010 (2001)

71. G. Corcella et al., Preprint hep-ph/0107071 (2001)

72. S. Bethke, J. Phys. G **26**, R27 (2000). Updated in S. Bethke, Prog. Part. Nucl. Phys. **58**, 351 (2007)

73. M. Wing (on behalf of the ZEUS Collaboration), in *Proc. of the 10th International Conference on Calorimetry in High Energy Physics*, ed. by R. Zhu, Pasadena, USA (2002), p. 767. Also in preprint hep-ex/0206036

74. S. Chekanov et al. (ZEUS Collaboration), Eur. Phys. J. C **21**, 443 (2001)